Passive Microwave Precipitation Retrievals Over Problem Surface Types: An Intercomparison

---

Author:
Nicholas J. Neutkens

Supervisor:
Dr. Grant W. Petty

A thesis submitted in partial fulfilment of
the requirements for the degree of

Master of Science
(Atmospheric and Oceanic Science)

at the

University of Wisconsin-Madison

August 2015

Thesis Declaration and Approval

I, Nicholas J. Neutkens, declare that this thesis titled, 'Passive Microwave Precipitation Retrievals Over Problem Surface Types: An Intercomparison' and the work presented in it are my own.

Nicholas J. Neutkens		
Author	Signature	Date

I hereby approve and recommend for acceptance this work in partial fulfillment of the requirements for the degree of Master of Science:

Grant W. Petty		
Department Chair	Signature	Date

Larissa E. Back		
Faculty Member	Signature	Date

Ankur R. Desai		
Faculty Member	Signature	Date

UNIVERSITY OF WISCONSIN-MADISON

Abstract

Department of Atmospheric and Oceanic Science

Master of Science

Passive Microwave Precipitation Retrievals Over Problem Surface Types: An Intercomparison

by Nicholas J. Neutkens

Over the last few decades, significant improvements have been made to rain-rate algorithms using the Tropical Rainfall Measuring Mission (TRMM) Microwave Imager (TMI), and the preceding microwave radiometer instruments. However, the current standard algorithm used by the National Aeronautics and Space Administration (NASA), called the Goddard Profiling (GPROF) algorithm, continues to display some erroneous rain signatures over troublesome surface types. An intercomparison between GPROF and the new University of Wisconsin (UW) algorithm is presented here, where over 300 individual case studies are visually observed and statistically compared for a variety of rain systems over different surfaces. Both algorithms are validated against the TRMM Precipitation Radar (PR). Results have shown that the UW algorithm is statistically outperforming the GPROF algorithm on a case-by-case basis, especially when observing precipitation over coastlines and deserts. Use of the Heidke Skill Score has demonstrated the UW algorithm's ability to more accurately detect very small rain rates compared to the GPROF algorithm.

Acknowledgements

First and foremost, I would like to extend my deepest gratitude and thanks to Dr. Grant Petty for providing me the opportunity to work as his graduate student for the past two years. Without his support and guidance this work would not have been possible. Among his own high pressure deadlines, he has taken the time to answer my many questions, and from the beginning of my graduate career, he has allowed me to work at my own pace. His scientific integrity will resonate with me in all of my future endeavors.

Next, I would like to thank all of my peers in the AOSS building for their help in solving challenging problems and for their time outside of work, which contributed immensely to keeping my stress levels tolerable during times of intense schoolwork and research. The experiences made with them will remain happily in my memories.

The funds I received from NASA Grant NNX13AG49G is the sole reason I was able to attend graduate school and complete my Master's degree. I am very thankful for the opportunity NASA has provided, as well as the data retrieved from the Goddard Earth Sciences Data and Information Services Center that allowed me to complete my research.

I would also like to extend my thanks to Dr. Chuntao Liu for conveniently providing me with the specific case studies used in this experiment. His curiosity for the performance of various rain rate algorithms pushed me in the direction of this research.

The feedback I have received from my committee members, Dr. Ankur Desai and Dr. Larissa Back, was highly valuable and greatly appreciated. I thank both of them for their time and commitment to helping improve this thesis.

Finally, to my parents Terry and Linda, and to the rest of my family for all of their love and support. Their words of encouragement during my most difficult struggles have truly paved the path toward all of my success, now and in the future.

Contents

List of Figures

List of Tables

Chapter 1

Introduction

1.1 Motivation

1.1.1 Energy and Hydrological Cycle

Obtaining quality measurements of precipitation on a large scale remains a challenge for scientists today. Precipitation is a key component in Earth's hydrological cycle as an important source of freshwater. The amount of precipitation that occurs is constrained by Earth's energy budget; therefore, the changing climate, which changes the energy budget, has a significant effect on the hydrological cycle and the location and intensity of rainfall (Trenberth, 1999, Meehl and coauthors, 2007, Trenberth et al., 2009). The precipitation from convective systems makes up a significant portion of the tropical atmospheric heating. In convective rain systems, the vertical distribution

of latent heat release affects many large scale tropical circulations, which in turn can affect midlatitude weather and determine cycles of droughts, floods, monsoons, hurricanes, etc, (Simpson et al., 1996, Tao and coauthors, 2001). The ability to observe instantaneous rain rates may be able to improve weather forecasts, and help determine storm tracks before they come in the range of detectability for ground based radars. We can also use observations of rainfall at larger timescales to help monitor drought conditions and flood risks (Jeyaseelan, 2003).

1.2 Measuring Rain

1.2.1 Rain Gauges and Radar

There are many ways in which rainfall can be measured. Rain gauges, which essentially just collect rain water, can get very direct measurements of precipitation; however there is a very uneven distribution of gauges on a global scale. There are also many sources of error for exact measurements due to wind, snowfall, evaporation, etc.

Ground based radars do a good job of obtaining rainfall data at regular time intervals. However, like rain gauges, there is very limited global coverage of ground based radars, especially over the ocean, in deserts, in mountain ranges, and for less developed parts of the world. The quantitative measurements associated with radar retrievals can

also be unreliable due to instrument calibration, range effects, interference, over-saturation of nearby intense systems, and variable reflectivity factor Z and rainfall rate R relationships (Creutin et al., 1988).

1.2.2 Satellites

A third way to estimate rainfall is using satellite observations from space. Visible (VIS) and infrared (IR) imagers aboard satellites are useful in determining where thick and deep clouds are present, which can be associated with rainfall. Unfortunately, the relationship between observing these clouds and finding an associated rain rate is unreliable, as IR methods will miss precipitation from warm-topped clouds, and may falsely observe rain from cold, thin clouds (Todd et al., 2001, Anagnostou et al., 1999). VIS methods are also unreliable since not all observed bright clouds will necessarily be raining.

Another method used to detect rainfall from satellites is through passive microwave (PMW) instruments. Over radiometrically cold and highly polarized regions like the ocean, PMW techniques take advantage of the increases in brightness temperature and decreases in polarization that occur from microwave emission due to liquid precipitation (Gopalan et al., 2010). In other words, the rain above oceans is not highly polarized, and emission from rain particles looks radiometrically warmer than the

ocean background. Over both land and ocean, sharp reductions in observed brightness temperatures can be seen when there are large ice particles aloft that scatter microwave radiation (Wang et al., 2009, Gopalan et al., 2010). Typically the scattering of ice particles is more observable over land, where the background is radiometrically warm.

A drawback to PMW techniques is that, relative to the antennae on satellites, microwave wavelengths are long, and as a result, they provide very poor angular resolution of small scale features. It is for this reason that PMW techniques are not viable on geostationary satellites, and are limited to low-Earth orbits.

In addition to PMW techniques, there have recently been active microwave radars implemented among newer satellites. The first was aboard the Tropical Rainfall Measuring Mission (TRMM) (Simpson et al., 1988, Kummerow et al., 1998, Kummerow and coauthors, 2000), the focus of this thesis. More recently a dual frequency active microwave radar was added aboard the Global Precipitation Measurement (GPM) satellite (Smith and coauthors, 2007), which launched in 2014. The active radars are used to detect the backscatter of microwave energy by precipitation sized particles in an observed column. The measurements from the radar are from direct echoes associated with rain, which implies that the overall precipitation measurements are unambiguous in nature. It also provides direct information about the vertical structure of the rain system. The drawbacks to this technique are that the radar is limited

to a smaller swath width than the PMW instrument, and it too can only function successfully in low-Earth orbits (Kummerow and coauthors, 2000).

Satellites that operate at low-Earth orbits (350-1000 km altitude) typically can only make a couple observations per day over a specific location. The spatial resolution from these satellites is usually very good because of their proximity to Earth, however that also implies that the satellite yields poorer spatial coverage.

Satellites in geostationary orbits (35,800 km altitude) have the means to make much more frequent observations, usually hourly or better, over a specific location. The improved frequency of observations is still limited to low and mid-latitude locations, and the large distance from Earth severely limits the spatial resolution.

Using the combined methods described above, the VIS and IR instruments on geostationary satellites, which have greater sampling, can be empirically calibrated for more robust measurements. Projects such as the Global Precipitation Climatology Project (GPCP) and the CPC Merged Analysis of Precipitation (CMAP) have combined datasets from low-Earth orbit microwave, geosynchronous IR, and rain gauge instruments to find that this method is reliable on annual scales, but involves some systematic variation on regional and seasonal scales (Huffman et al., 1997, Xie and Arkin, 1997).

1.3 Physical Basis for PMW Rain Rate Estimation

At microwave frequencies, the atmosphere is relatively transparent to microwave radiation (Evans et al., 1995). In scenarios with no precipitation, brightness temperatures observed from space are determined by surface emission and atmospheric contributions to emission by water vapor, cloud water, and oxygen (Liebe et al., 1993).

Land characteristics typically include high, weakly polarized emissivities. The emissivity depends mainly on soil type, vegetation cover, soil moisture, and snow/ice (Grody, 1991). Oceans, on the other hand, have very low, strongly polarized emissivities (Weinman and Guetter, 1977, Wilheit et al., 1977).

The atmospheric contribution due to water vapor is most noticeable near 22 GHz and for frequencies greater than 50 GHz (Petty and Katsaros, 1992). There is another particularly strong absorption band for water vapor at 183 GHz. This channel was included on GPM; however it is not available on TRMM. The cloud contribution tends to increase with higher frequencies. It is relatively weak at 10 GHz, and very strong at 85 GHz. For any given channel, the contribution from oxygen remains nearly constant on a global scale.

When precipitation is present, interactions with microwave radiation becomes much more apparent at microwave frequencies. This occurs for a variety of reasons including: the increased amount of condensed water in the observed column, much larger particle

sizes corresponding to rain and ice, the absorption and emission characteristics of raindrops, and large ice particles scattering radiation (Petty, 1995).

Combining this physical background implies that each microwave frequency channel has its own characteristic response when observing precipitation relative to surface and atmospheric contributors. For example, depolarization and increased brightness temperature values over oceans is frequency-dependent, as is the temperature reduction associated with radiation scattering by ice particles (mainly over land).

Each channel is also prone to observe geophysical "noise" resulting from variations in background emissivity and polarization. This "noise" can be exacerbated by certain surface types, such as snow, and desert sand, which can have a similar scattering effects as compared to ice, which in turn can lead to false rain signatures. It is thus the goal for retrieval algorithms to exploit the combined information from multiple channels to distinguish between actual rain signatures and the potential geophysical noise as well as possible.

The satellite instrument observes the combination of radiation intensity from the ground and atmospheric components, and radiative transfer models may be used to compute a brightness temperature (Johnson et al., 2012). Each of the microwave channels have varying responses to atmospheric variables including ice particles, rain water, water vapor and cloud water (Petty, 1994a, Johnson et al., 2012).

When observing rainfall over the ocean, water drops are strong emitters of radiation,

and therefore warmer brightness temperature conditions are observed by the satellite. When larger particles such as ice are present, microwave radiation tends to scatter, and the observations from the satellite exhibit depressed brightness temperatures (Petty, 1994a).

Conditions on the ground also contribute to what the satellite observes. Coarser particles such as snow and sand have similar scattering properties to ice present in convective clouds (Smith et al., 1992). When scattering alone is the basis for detecting rainfall, surface scatterers can yield false rain signatures. A major problem in the estimation of over-land precipitation, and one the University of Wisconsin (UW) algorithm attempts to address, is the optimal detection of precipitation in the presence of such difficult surface types.

1.4 History of Satellite PMW Rainfall Estimation

1.4.1 Early Days

Since the 1970s, satellites have used passive microwave techniques to observe precipitation from space. The first of these microwave instruments was launched aboard the Nimbus 5 satellite in December, 1972 (Wilheit et al., 1976). In the early stages of instrument development, the focus was on detection of precipitation over the ocean in order to better understand the location and extent of rainfall where it was unable

to be observed reliably beforehand. The Nimbus 5 satellite had only one channel, 19 GHz (horizontally polarized), with which to observe precipitation.

One of the first quantitative measurements of rainfall was by using the Nimbus 5 satellite (Wilheit et al., 1977). Changes in 19 GHz brightness temperatures were assumed to be associated with different rain rates. The paper compared their findings with rain gauge and radar data, and they were able to verify the assumption.

The launch of the Nimbus 6 satellite introduced two channels of 37 GHz with horizontal and vertical polarizations. Weinman and Guetter (1977) were able to associate brightness temperature changes with different polarizations in the 37 GHz channel for land and ocean rain rates. It was noticed here that oceans were strongly polarized, whereas land was not, and a linear combination of the two channels, or 'polarization correction', was implemented to help eliminate the contrast between ocean and land while preserving sensitivity to scattering due to convective precipitation. Similar filtering was implemented in many subsequent algorithms (Spencer, 1986, Spencer et al., 1989, Conner and Petty, 1998), and is the forerunner of the UW algorithm.

1.4.2 SMMR

In 1978, the Scanning Multichannel Microwave Radiometer (SMMR) was launched aboard the Nimbus 7 satellite and measured brightness temperatures until 1987. This instrument contained 10 dual-polarized channels at five frequencies ranging from 6.6

GHz to 37 GHz. The main use of this instrument was to gather information on sea surface temperature and wind stress, but precipitation was also observed (Gloerson and Barath, 1977). Examining SMMR images over the US, Spencer et al. (1983) observed that cold brightness temperatures were evident during heavy precipitation in the 37 GHz channel over land and that brightness temperatures were apparently affected by ice aloft. This observation led to the emergence of scattering-based algorithms in addition to the emission-based approach pioneered by Wilheit et al. (1977) and others used today. He also noticed retrieval biases in the rain rate/brightness temperature relationship that was first observed by Wilheit et al. (1977). This would later be named the "beam filling effect" (Chiu et al., 1990).

1.4.3 SSM/I and SSM/IS

In 1987, the Special Sensor Microwave Imager (SSM/I) launched aboard the F-8 satellite as a part of the Defense Meteorological Satellite Program and led to a variety of experiments (Adler et al., 1991, Smith et al., 1992, Barrett and Coauthors, 1994). The SSM/I is still taking measurements today and includes microwave channels at 19.35, 22.235, 37.0, and 85.5 GHz. All but the 22 GHz channel is dual-polarized, and the new 85 GHz channel exhibited higher sensitivity to scattering ice particles. SSM/I travels in a near polar, sun-synchronous orbit. A successor instrument called the SSM/I Sounder (SSM/IS), which added various sounding channels, was first launched in 2003. There are currently three DMSP satellites equipped with SSM/IS instruments.

A plethora of algorithms were developed for the SSM/I, and a variety of intercomparison projects were performed including the Precipitation Intercomparison Projects (PIP) (Barrett and Coauthors, 1994, Smith and coauthors, 1998, Adler et al., 2001), and the Global Precipitation Climatology Project (GPCP) Algorithm Intercomparison Projects (AIP) (Barrett and Coauthors, 1994, Ebert et al., 1996, Smith and coauthors, 1998, Adler et al., 2001, Schols et al., 1999).

Results from Grody (1991) gave rise to the Scattering Index (SI) parameter, which is used to identify scattering surfaces and obtain estimates of rain rate, snow-equivalent water content, and many other parameters.

At this point some algorithms implemented a cloud/radiative transfer model-based approach to rigorously compute the rain rates associated with brightness temperatures (Mugnai and Smith, 1988, Smith et al., 1992, Kummerow et al., 1989, Kummerow and Giglio, 1994a). The Kummerow et al. (1989) paper is one of the first to implement a Bayesian approach to compute rain rate, which will be discussed in a later section. In Petty (1994a), an inversion-based algorithm was developed that, instead of relying on computationally demanding cloud/radiative model calculations, combined raw brightness temperatures and retrieved water vapor and wind speed fields to determine scattering and polarization indices, that in turn were used to perform an iterative search for a rain field consistent with 19.35 and 37.0 GHz polarizations.

In Conner and Petty (1998), three algorithms, attempting to separate rain signatures

from background variability over land, were tested against two quasi-standard algorithms developed at NASA and NOAA. The algorithms were able to successfully show that utilization of monthly maps of mean radiance instead of location independent algorithms were more reliable in detecting lighter precipitation over land.

Of the above, the Bayesian approach used by Kummerow et al. (1989) would eventually evolve into the algorithm that is currently used as the standard for most PMW imagers, whereas the Conner and Petty (1998) approach can be considered an early predecessor of the University of Wisconsin (UW) algorithm that is the focus of this thesis.

1.4.4 TRMM

1.4.4.1 Satellite Mission

The Tropical Rainfall Measuring Mission (TRMM) was launched in 1997 with the sole purpose of detecting precipitation via active and passive microwave instrumentation over the tropics from 38°N to 38°S (Simpson et al., 1988, Kummerow et al., 1998). The active instrument, called the Precipitation Radar (PR) is the first spaceborne active microwave radar. The PMW instrument called the TRMM Microwave Imager (TMI) was essentially an SSM/I instrument with added 10.7 GHz dual polarized channels. Originally intended as a three-year mission, the instrument survived four years at its

original altitude of 350 km, and an altitude boost in the later half of 2001 increased the lifetime for an additional 14 years until the on board fuel was depleted in mid-2015.

The TMI has a swath width of approximately 880 km on the surface of the Earth. The swath for the 10.7, 19.4, 21.3, and 37 GHz contains 104 pixles per scan, and the 85 GHz which has better spatial resolution has 208 pixels per scan (Kummerow et al., 1998). The microwave instrument also has a conical scan of 130° and scans with an off-nadir incident angle of 52.8°. The PR has a swath width of 247 km and uses the active technique described previously to determine the vertical profiles of rain and snow looking straight down (nadir). The Visible and Infrared Scanner (VIRS) aboard TRMM observes cloud top temperatures in the infrared and visible parts of the electromagnetic spectrum. It has a swath width of 833 km and observes the surface at nadir.

1.4.4.2 Goddard Profiling Algorithm Methodology

The rainfall product that is currently accepted and used by NASA is based primarily on the Goddard Profiling (GPROF) algorithm. Throughout TRMM's extended lifetime, the GPROF algorithm has been improved upon from time to time, and the most up to date version is known as the 2A12 version 7, or 2A12 V7. Work on this algorithm began before the launch of TRMM (Kummerow et al., 1989), and prior to updated versions the algorithm relied solely on a synthetic database that was constructed from radiative transfer calculations applied to cloud resolving models. The

algorithm implements a basic Bayesian approach with respect to precipitation retrieval in that it searches a large database of rain rates associated with the observed brightness temperature (Kummerow and coauthors, 2001, Kummerow et al., 2011).

The theoretical Bayesian approach designed to determine a particular rain rate given an observed multichannel vector of brightness temperature, $Pr(R|\mathbf{T}_B)$, and applied to the GPROF algorithm can be written as

$$Pr(R|\mathbf{T}_B) = Pr(R) \cdot Pr(\mathbf{T}_B|R), \tag{1.1}$$

where $Pr(R)$ is the climatological probability that a particular rain rate profile R will be observed, and $Pr(\mathbf{T}_B|R)$ describes the probability of observing a particular brightness temperature given a rain rate R. Equation 1.1 is described in terms of continuous functions; however the relevant probabilities of rain rate are derived from a large database that is constructed from discrete matches between $\mathbf{T}_B$ and R (Kummerow et al., 2011). In other words, when a brightness temperature is measured by a satellite, a large database of rain rates associated with that temperature are searched for and averaged to produce an estimated rain rate. The current version of GPROF no longer requires synthetic data, and now contains 7+ years of PR-TMI matchups that are used to populate the observational database, yet there is still strong evidence of problems detecting precipitation over various surface types (Sudradjat et al., 2011, Ferraro and coauthors, 2013).

In all versions of GPROF, a nine-dimensional channel space must be adequately populated by rain rate solutions associated with observed brightness temperatures and it must also correctly specify the match tolerances and/or channel weights in the channel space. While this method can be effective, there also many factors that may lead to difficulty in measuring rain over varied surface types.

The main issue with this approach is that the adequate population of nine-dimensional channel space can be very difficult to achieve. The nominally Bayesian approach means that given an observed brightness temperature, the entire multi-channel database must be searched in hopes of finding an associated rain rate. There is rarely a rain rate associated with one specific brightness temperature vector, so to ensure the selection of a rain rate value, the approach is to provide a small range of brightness temperatures given the observed, then using a weighted average of selected rain rate values in that range to produce a rain rate. If the brightness temperature range is too small, the algorithm might find no matches. If the range is too large, then the precipitation information loses accuracy because too many scenes are included that are not necessarily good matches to the observations. GPROF also assumes diagonal covariance of the background noise, which can lead to false signatures (Petty and Li, 2013a). Within the nine-dimensional space, the geophysical variance can produce erroneous results.

1.4.5 GPM

A little over a year before TRMM shut down, a new Global Precipitation Measurement (GPM) satellite was launched in February 2014. The GPM mission goals are very similar to those of TRMM, except the geographic range of measurements increased to cover 60°N to 60°S, and four more channels were added: 166 GHz with vertical and horizontal polarization and 183 ± 3 GHz vertical and 183 ± 7 horizontal (Smith and coauthors, 2007). The higher latitudes covered by GPM makes precipitation estimation more challenging because of surface snow and ice, as well as the generally lighter rain rates that occur in those regions. The added higher frequency microwave channels are more sensitive to the snow/ice effects. (Smith and coauthors, 2007). The main focus of this research involves measurements from the TRMM satellite, and any success can hopefully be applied to GPM.

1.5 Remaining Difficulties

While considerable progress has been made with PMW remote sensing of precipitation, observing very light rain rates, especially over various surface types and coastlines, is still problematic for many algorithms (Gopalan et al., 2010, Ferraro and coauthors, 2013). The inherent problems that come with detecting precipitation over land using passive microwave techniques can be directly related to observations over different terrestrial surface types and the associated transitions in emissivity. Over

land, microwave retrieval methods are less direct in that they rely more heavily on ice scattering aloft in convective systems to determine a surface rain rate (Vivekanandan et al., 1990, Smith et al., 1992, Petty, 1995). The majority of this signal is detected using the 85 GHz channel and depends on ice particle sizes and shapes, ice particle number concentration, and the amount of supercooled liquid associated with ice. If there is no ice scattering aloft, differences between the background land observations and potential rain signal cannot easily be determined, and the corresponding brightness temperatures might not accurately correlate to the occurring rainfall. In addition to stronger emissivities, each channel on the instrument has a different footprint size, which means a different fraction of land is measured for each channel, and the combined information is prone to yielding erroneous rain rates.

A variety of techniques have been attempted by other algorithm developers in order to minimize precipitation rate errors. For example, instead of using a straight brightness temperature threshold to determine associated rain rates, a polarization corrected temperature cutoff threshold has been developed and shown to increase the estimated rainfall over coasts in the tropics (McCollum and Ferraro, 2005). Other improvements have been observed by essentially removing the surface classification screening step within the algorithm, and instead using ancillary datasets to determine surface types. This method has in some cases reduced the misclassification of surface types that usually result in erroneous rain signatures (Sudradjat et al., 2011).

1.5.1 UW Algorithm

The UW algorithm was recently developed by Professor Grant Petty at the University of Wisconsin-Madison (Petty and Li, 2013a) and seeks to use a surface-blind retrieval method combined with a database dimensionality reduction (Petty, 2013) to improve rain rate measurement accuracy over all surface types. The surface-blind approach, unlike GPROF, does not require knowledge of surface emissivity, but instead relies on a mean and covariance of background brightness temperatures over a well-defined fraction of Earth's surface. Using the dimensional reduction approach, the UW algorithm seeks to identify rain signatures orthogonal to the background variability.

The goal of the dimensional reduction process is to reduce the GPROF nine-dimensional search space to a more reasonable and more adequately populated three-dimensional space using a two-stage principal component analysis (PCA) technique. A more in depth explanation of the procedure can be found in Petty (2013). Results from the two-stage PCA extracts most of the sensitivity to rain variance, and the most relevant data remains in the first few "pseudochannel" byproducts. Approximately 95% of the desired precipitation information is contained within the first three pseudochannels, which means the remaining six pseudochannels can be discarded without any significant loss of information.

After the completion of the PCA a newly created empirical database, based on TMI-PR matchups, is constructed with the weighted averages are precomputed and stored

within a lookup table. Given an observed brightness temperature, the pre-constructed lookup table is simply searched for corresponding rain rates. The main difference between the UW and 2A12 V7 algorithms is that the three pseudochannels are much more densely populated, implying a much more robust representation of precipitation rates. An additional product from this method is the ability to construct a reliable posterior probability distribution function (PDF) for a variety of selected rain rate thresholds. The PDF is constructed with 16 logarithmically spaced thresholds measured in millimeters per hour: 0.0, 0.01, 0.02, 0.03, 0.05, 0.1, 0.2, 0.3, 0.5, 1.0, 1.7, 3.0, 5.2, 10.0, 17.0, and 30.0 (Petty and Li, 2013a). However, the PDFs are not relevant to the present study and will not be considered further.

1.5.2 UW Performance

Comparisons between the 2A12 V7 and UW have already been studied to some extent. In Petty and Li (2013b), a global validation and intercomparison was completed through the evaluation of annual total precipitation as well as ability to retrieve instantaneous pixel-level rain rates. Seven separate surface classes were analyzed, and for total annual precipitation, each surface class displayed significantly reduced bias and RMS error in the UW product. The instantaneous skill at observing light rain rates over troublesome surface types also presented strong improvements.

1.6 Remaining Questions

It has been observed that the UW algorithm more reliably computes precipitation rates on an annual scale; however observations on a case-by-case basis have yet to be evaluated. Detailed case studies over troublesome surface types can provide insight about the following questions: How does each algorithm perform in a given situation? How often does one algorithm outperform the other? In the following intercomparison over 300 specific case studies are analyzed over a large variety of surface types and locations in an attempt to confirm and discover observational and statistical differences between 2A12 V7 and the UW algorithm.

Chapter 2 explains more about the cases/data used and how they were chosen. The comparison methods are described in Chapter 3. Chapter 4 contains the results and analysis, and Chapter 5 provides conclusions and gives insight into future work.

Chapter 2

Data

2.1 Cases

A large variety of specific case studies were independently chosen for an informal algorithm intercomparison by Dr. Chunato Liu, Texas A&M University, in order to get a robust representation for different combinations of precipitation over all surface types (Chuntao Liu, personal communication). Dr. Liu generously shared his case selections with us for use in the present analysis. The case studies selected were separated into three different rain type categories including deep mesoscale convective systems (MCS), shallow MCS, and isolated deep convective systems (ICS). These categories are defined as follows:

-Deep MCS is defined by a system area greater than 20,000 km^2, and a maximum echo top height greater than 12 km.

-Shallow MCS is defined by a system area greater than 6000 km^2, and a maximum echo top height less than 8 km.

-ICS is defined by a system area of less than 1000 km^2, and a maximum echo top height greater than 12 km.

Multiple occurrences of these rain types are further delineated into nine different locations including: Central Africa, Amazon region, Southeast United States (SEUS), Southwest United States (SWUS), Argentina, Indian region, China, Maritime Continent, and Australia. In addition to these regions and rain categories, multiple precipitation events over the Sahara Desert, snow-covered land, snow over ocean, warm rain over land, and mountain cases were considered. A final count of over 300 specific rain cases over different locations were observed during this experiment.

It has previously been mentioned that UW and 2A12 comparisons have been made on an annual scale (Petty and Li, 2013b). The intent of this experiment is to examine algorithm differences on a case by case basis. The selections have not only been made to observe which algorithm performs better, but also to find particular surface types for which both algorithms need improvement.

2.2 Overview

The algorithm intercomparison depends on time-, space-, and resolution- matched pixel level rain rates for each of the chosen cases. These are obtained from the following three products:

(i) The NASA standard GPROF algorithm for TMI. Also known as 2A12 version 7;

(ii) The new UW algorithm also for TMI described by Petty and Li (2013a), and

(iii) the surface rain rates estimated by the PR-derived product, also known as 2A25.

For the purposes of this experiment, the UW and GPROF products are compared directly to the much more reliable 2A25 product; however it is understood that the radar-derived product is still subject to errors, especially when shallow, light, and frozen precipitation is present.

In addition to the previously described intercomparison products, the three pseudochannels, derived from the original nine TMI sensor channels (Petty, 2013), for each swath will be displayed for visual comparisons of variance and associated rainfall, as well as the 85 GHz vertically polarized (85V) and 37 GHz horizontally polarized (37H) channels. The 85V channel is most associated with highly convective systems and ice scattering aloft, meaning very low brightness temperature values should be associated with higher intensity rain rates on the corresponding TMI and PR swaths

(Gopalan et al., 2010). The 37H channel responds to emission by liquid precipitation over an ocean background.

2.3 Resolution Matched PR

In order to properly compare the rainfall data from UW and GPROF algorithms, the resolution differences must be taken into account. The PR detects precipitation with much higher resolution than the TMI, thus comparisons must be performed after the rainfall data from the PR is averaged to approximately the same resolution as the TMI. This was accomplished by extracting the PR rainfall data combined in each TMI footprint and performing a weighted average of rainfall values with the most weight considered closest to the center of the TMI measurement. Using an exponential weight function, a weighting coefficient was determined based on the TMI resolution of 27.5 km at 19 GHz. Then the coefficient was used to calculate the weight of a given pixel based on its distance to the center of the footprint. The results from the weighted average show a much more blurred signal by the PR that is comparable to TMI resolution.

2.4 VIRS

The VIRS is a visible and infrared imager that provides a conventional view of clouds. Our concern here is with IR imagery near 11 μm which permits us to view clouds without respect to day or night. The VIRS data retrieved from the NASA server displays the channel values in units of milliwatts per centimeter squared per micrometer per steradian. In order to convert the IR channel measurements into values of brightness temperatures for plotting purposes, it is necessary to invert the Planck's function as follows

$$T_B = \left[\ln \left(1 + \frac{2hc^2}{I_\lambda \lambda^5} \right) \frac{k_B \lambda}{hc} \right]^{-1}, \tag{2.1}$$

where I_λ is the reported intensity, k_B is Boltzmann's constant, h is Planck's constant, c is the speed of light, and λ is the chosen wavelength. With this conversion, we can display images of IR brightness temperature for selected swaths in order to capture the cloud cover over the observation regions.

Chapter 3

Comparison Methods

3.1 Heidke Skill Score

Once the data have been averaged for resolution comparability, a variety of statistical analysis can be properly performed. A preview of the statistical methods are described in this section starting first with the Heidke Skill Score (HSS) (Heidke, 1926, Doswell et al., 1990). The main goal of the HSS is to determine the reliability or skill of an algorithm or forecast given a series of binary variables. The HSS is defined quantitatively as

$$HSS = \frac{2(AD - BC)}{(A + C)(C + D) + (A + B)(B + D)} \tag{3.1}$$

t

TABLE 3.1: Contingency table entries used in the computation of the Heidke Skill Score.

	Observed	
Forecast	No	Yes
Yes	B	A
No	D	C

in which the variables in Eq. 3.1 are defined by the contingency table shown in Table 3.1. Once all values are determined, the skill score can be computed and will produce some value from -1 to $+1$. A value of $+1$ describes perfect skill in forecasting, -1 implies complete negative skill where no information is correctly predicted, and 0 meaning that all values are essentially random whether or not they are predicted correctly.

In the context of this experiment, the HSS can be utilized to determine the skill of each algorithm at determining a rain versus non-raining pixel as compared to the radar-derived validation product; however we can take this process a step further according to Conner and Petty (1998), and use the HSS to retrieve an algorithm's skill at predicting a rain rate that exceeds a particular threshold of intensity $R_{1,0}$ in the validation rain rate R_1. This implies that the HSS is now a function of the arbitrary rain rate threshold selected.

Using the HSS dependent on a rain rate threshold is valuable in determining the skill of each algorithm over problem surface types. Specifically, it can be used to

determine the lower limit of rain rate detectability and can be compared to higher threshold values over the same surface types. This evaluation is very useful since the aim of this experiment is to show the improvements in rain rate measurements from the UW algorithm over surface types that have historically produced problems for passive microwave instruments.

The procedure in determining the HSS begins with a scatter plot of rain rates measured by an algorithm in question (either UW or GPROF) and the corresponding validation 2A25 rain rates. Any selected pair of rain rates will split the scatter plot into four quadrants that correspond to the A, B, C, and D values in Table 3.1. Different threshold values will produce different skill values. In this experiment we will focus on comparing two different thresholds: 1.0 mm hr^{-1} and 0.1 mm hr^{-1}. The first threshold is selected for the reason that the score did not significantly improve above that value, and the second threshold is selected as an arbitrary very low limit value that can be used to easily compare each algorithm's skill at detecting small rain rates.

3.2 Conventional Validation Statistics

The other comparison methods used to evaluate the results of this experiment are fairly standard and include calculations of root mean square (RMS) error, mean ratios, and Pearson correlation coefficients.

The RMS difference is traditionally used to characterize the typical difference between values that are predicted by a model, or in this case estimates by TMI or GPROF, and values that are actually observed or considered truth, or in this case the values detected by the radar-derived 2A25 product. The result essentially contains an understanding of a sample standard deviation between forecasted and observed values. The mean ratio is simply the quotient of the means of the algorithm data and the PR data.

The Pearson product-moment correlation coefficient r is used as a measure of linear dependence among two variables. For this experiment, r is used to determine the linear correlation between the satellite-derived PR measured precipitation and the GPROF and new UW algorithms. Similar to the HSS, possible values for r range from $+1$ to -1, where $+1$ implies complete positive perfect correlation, 0 implies no correlation, and -1 implies complete negative correlation (Pearson, 1895). Unlike the RMS difference, the correlation coefficient is unaffected by systematic bias, so it is a better measure of the purely random component of the difference.

3.3 Other Constraints

It is conventional for most experiments involving the detection of rainfall via TRMM to omit the rain signatures that have a probability of occurring less than 50%. This probability threshold is calculated by GPROF and applied to the 2A12 V7 data, and the posterior PDF described in Petty and Li (2013b) is applied for this threshold in

the UW data. The particular case studies shown in this paper are displayed on 10° latitude by 10° longitude maps; however the statistically calculated data includes precipitation measurements from the swath slightly outside this range to no more than ±5°(the value varies for each event). This is chosen to be the case so we may include combined statistical intercomparisons of the main element in question (eg. strongly convective event) and the surrounding, possibly less intense precipitation events in order to get a robust understanding of the performance for the algorithms in question.

Chapter 4

Results

4.1 Selected Cases

After visually examining over 300 swaths over a variety of locations including depictions of the new UW algorithm, GPROF 2A12 V7, the PR, pseudochannels, and the chosen 37H and 85V frequency channels, a select few cases are chosen to present in this paper. The chosen cases are meant to represent particular dramatic instances where one can visually interpret the better performance of either the UW or GPROF algorithm. Those selected include a deep MCS over China, deep MCS over Australia, shallow MCS over Central Africa, shallow MCS over Australia, snow over land in China, warm rain over land in the Middle East, mountains in South China, and a Sahara Desert rain event on the border of Algeria and Niger. Swaths of each case will

be shown in the following format: Left column: UW algorithm calculated rain rate, 2A25 (PR) derived rain rate, 85V native resolution brightness temperatures, 37H native resolution brightness temperatures; Right column: GPROF 2A12 V7 calculated rain rate, and pseudochannels 1-3. We begin with a subjective discussion of the observed features. In the following section, the statistics for all representative cases will be discussed.

4.1.1 VIRS Images

Before delving into the specific case study TMI images, the (VIRS) swaths for each case are shown in Fig 4.1. This image is used to further interpret some of the TMI images since VIRS is able to distinguish the range of cloud cover over the observation area. We can use the cloud information to analyze whether or not a rain event might have been occurring or not based on the temperatures within that region. Each swath is titled with its TRMM orbit number, and the proceeding TMI images go in order of the swaths shown in Fig. 4.1.

4.1.2 Deep MCS China

The first case discussed here is categorized as a deep MCS over eastern China and the respective swaths are shown in Fig 4.2. This northern location was observed in mid-January, which may provide context for difficulty in retrievals due to potential snow

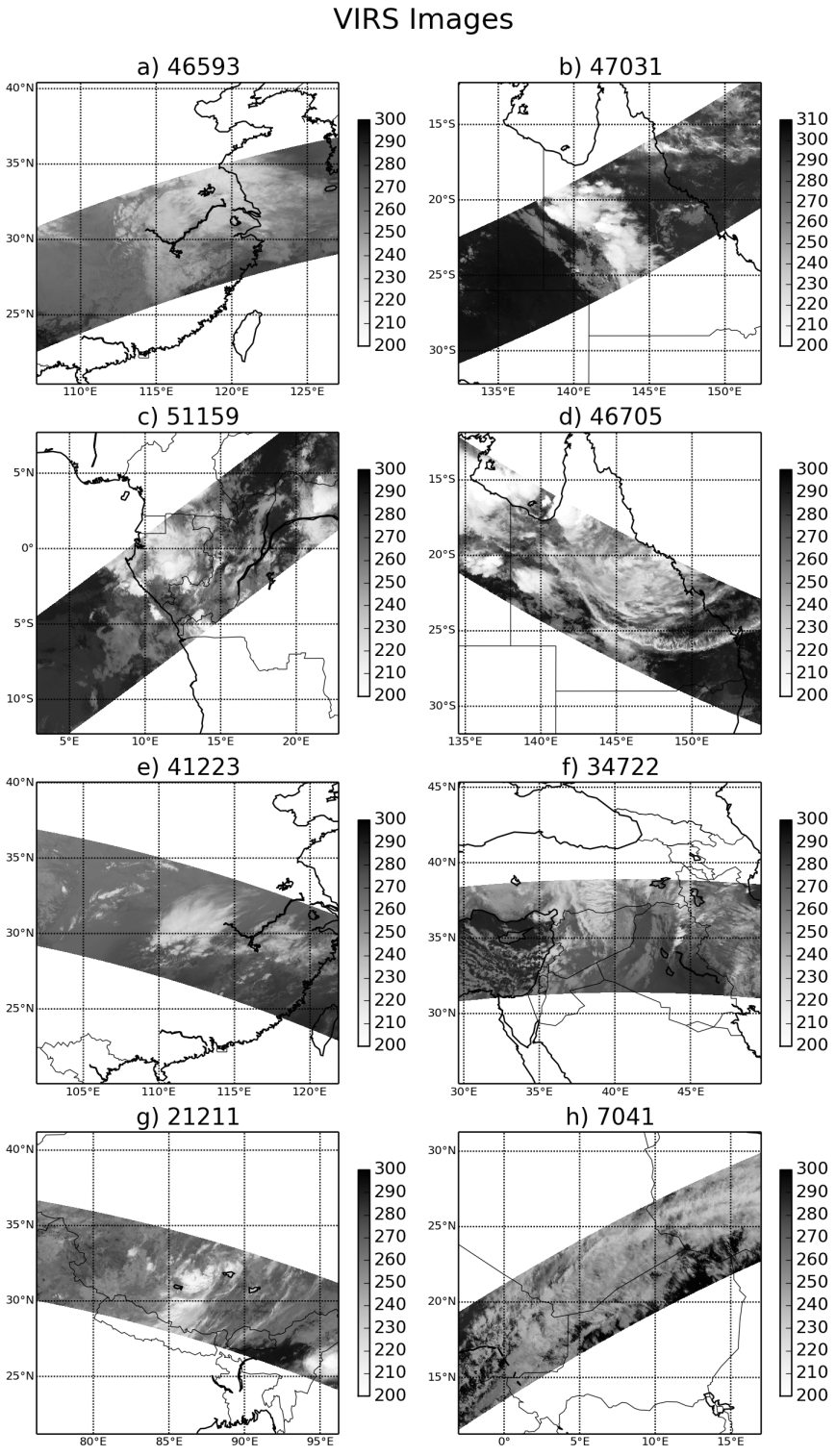

FIGURE 4.1: VIRS swaths displaying infrared temperatures (K) for the cases selected for further interpretation. Colder temperatures are associated with higher clouds. Swaths are labeled by TRMM orbit number.

or intense temperature gradients. An initial observation simply shows significantly more precipitation activity occurring from the UW algorithm than in 2A12. The UW algorithm compares nicely with the PR product, yet excludes some light precipitation in the western edge of the swath. The 2A12 product misses much of the precipitation occurring around the Yangtze River as well as the light precipitation on the western edge of the swath. Light rain rates along the coast are highly overestimated by 2A12 signifying the difficulty in smoothing out the sharp background temperature gradients associated with warm land and cool ocean. Coastal artifacting in 2A12 is evident and some small rain rates over the ocean are displayed that do not occur in the PR near the north east edge of the swath. The UW algorithm, which seems to retrieve most information over land, picks up minimal rain over the coast and ocean.

The 85V native resolution brightness temperatures displays coldest temperatures near the Yangtze River, and both the PR and algorithms have the highest associated rain rates in this region. Pseudochannel 1 and 2 also display the most variance in this region. The 85V channel also shows a sharp ocean temperature gradient which the pseudochannels have successfully filtered away as background variance, yet 2A12 shows some rain occurring that does not show in the PR. The 37H channel observes some warm spots over the ocean, most likely associated with rain drop sized particles. The warmest sections in the 37H are being represented by both algorithms as light rain.

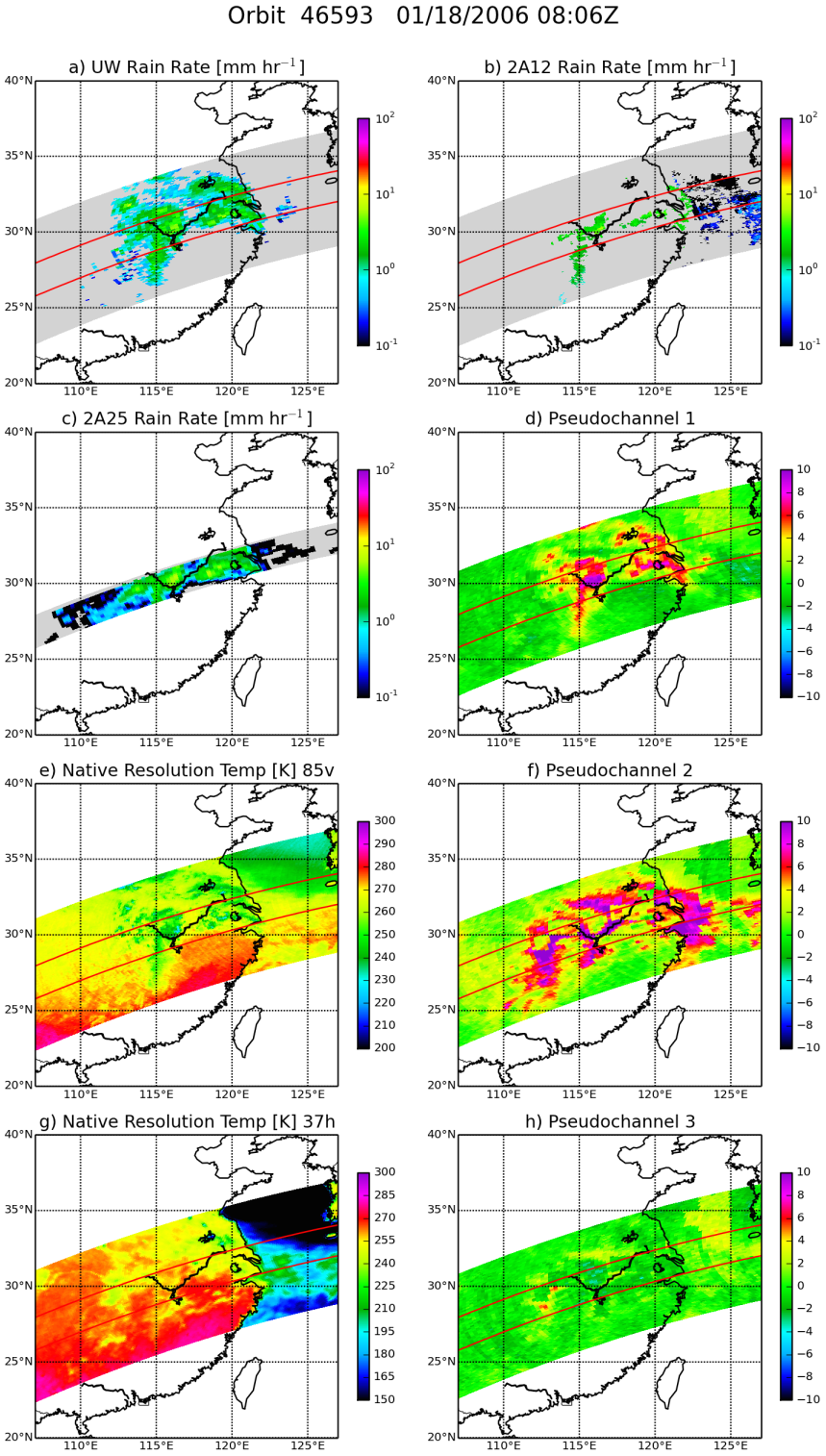

FIGURE 4.2: Swaths for Deep MCS over China. TRMM orbit 46593.

4.1.3 Deep MCS Australia

The next case includes a deep MCS over the north eastern part of Australia and is shown in Fig. 4.3. The immediate concern with this case is that we are observing precipitation over a very warm background, and minimal convective areas may be difficult to detect. Similar to the previous case, UW displays more of the spatial rain associated with the PR than does 2A12. An additional small system of rain is shown to the east of the main system in the PR that is not displayed in the UW interpretation, yet has a small presence in the 2A12. Offshore, 2A12 seems to be picking up more precipitation than UW, however both algorithms seem to collect an accurate depiction of ocean rain compared to the PR.

85V brightness temperatures are markedly depressed near the center of the main precipitation event and is associated with the highest rain rates for both algorithms. 2A12 overestimates the rain rate associated with the lowest temperatures significantly, yet almost ignores the lighter rain rates surrounding the deepest part of the system. Pseudochannel 1 shows large variance near the central event, and where rain is occurring over the ocean. 37H warm brightness temperatures offshore correspond accordingly to the rain observed by UW and 2A12. This case represents a good example of each algorithm's ability to detect highly convective rain events over a very warm background.

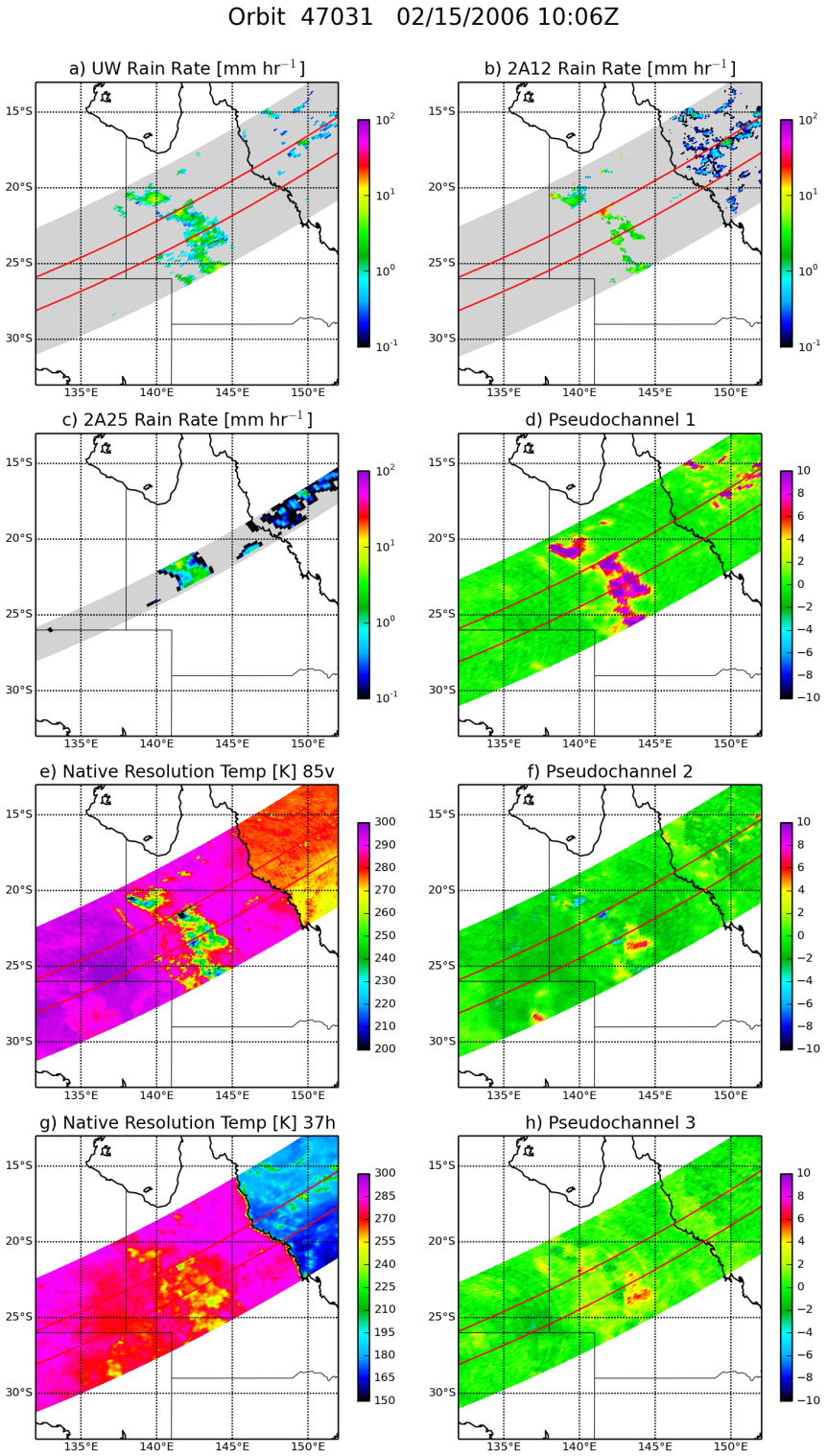

FIGURE 4.3: Swaths for Deep MCS over Australia. TRMM orbit 47031.

4.1.4 Shallow MCS Central Africa

As mentioned in the introduction, deep MCS systems are traditionally easier for rain rate algorithms to calculate precipitation due to the significant scattering of ice above warm surfaces, so we move on now to a shallow MCS over the west coast of Central Africa shown in Fig 4.4. The different radiative properties between land and ocean come into effect here. Focusing over land first, there is visible and continuous precipitation in the center of the PR swath with light rain rates observed between two, more intense systems. Both the 2A12 and UW pick up a majority of this precipitation, however the lighter rain observed in the PR is missed by both algorithms. In fact, both algorithms seem to be performing similarly over land. Taking a closer look at the coast, the PR displays another continuous band of precipitation that is evident with a few missing pixels in the UW interpretation, and not observed very well by 2A12. There are strong signatures of coastal artifacting (lack of raining pixels) along the coast for 2A12, where typically a strong temperature gradient forces the algorithm to ignore calculations in the region. The UW also misses some coastal precipitation, but artifacting does not visually seem to pose any problems as the gradient is filtered out by the pseudochannels.

When looking at the 85V channel, there are a couple of significant cold spots on the coast that 2A12 is able to distinguish as rain, but the pseudochannels are able to extract more variance from the background noise to produce a larger spatial area of rain detection. 2A12 is also calculating some small rain rates over the ocean near 9°E

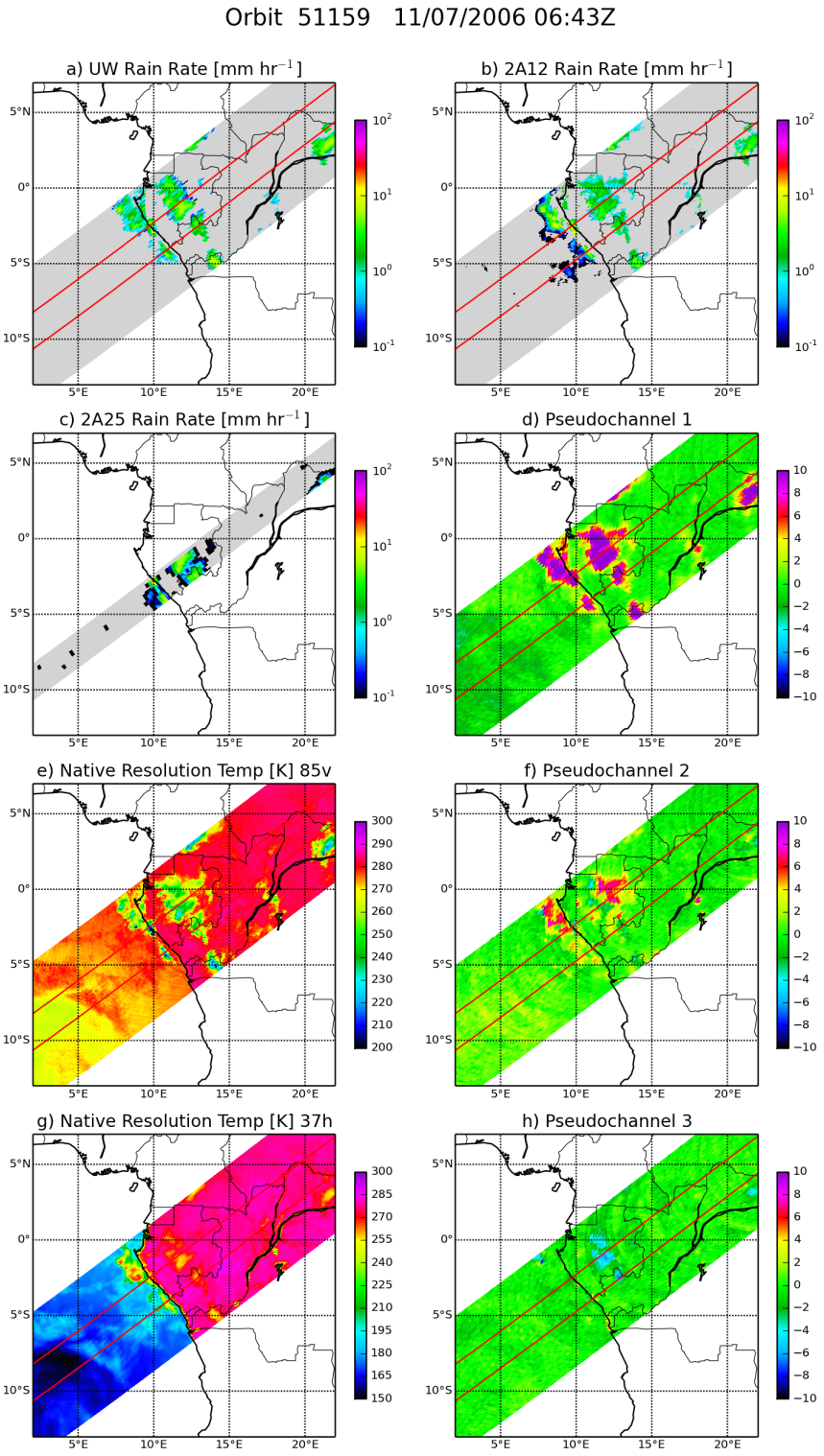

FIGURE 4.4: Swaths for Shallow MCS over west coast of Central Africa. TRMM orbit 51159.

6°S that is not evident in either the PR or UW. The 37H channel shows some warm temperatures over the relatively cooler ocean, however since no signal is observed in the PR, this can most likely be attributed to cloud water, which can be observed in Fig 4.1c, that 2A12 determined falsely as rain.

4.1.5 Shallow MCS Australia

Another shallow MCS event in the north east part of Australia is described next and shown in Fig. 4.5. Once again, the warm background and scattering properties of sand might affect the outcome of this case. During this event the PR shows lighter precipitation near the center of the swath and slightly heavier rain to the northwest. The rainfall occurring in the center of the swath is apparent in UW, however the rain rate is slightly overestimated. More surprising is that 2A12 displays very few pixels of precipitation in the region where rain activity is apparent. Overall the 2A12 displays much fewer raining pixels in the entirety of the swath compared to UW and PR. In the most north west corner of the swath, UW again interprets some higher rain rates compared to the PR, whereas the 2A12 calculates rain rate values closer to what the PR detects.

Small cold spots north west of the central activity in the 85V correspond to the small spatial area of rain displayed in the UW swath. 2A12 missing a majority of the central and surrounding rain activity represents a good example of the difficulty for the algorithm to search the nine-dimensional channel space for brightness temperature rain

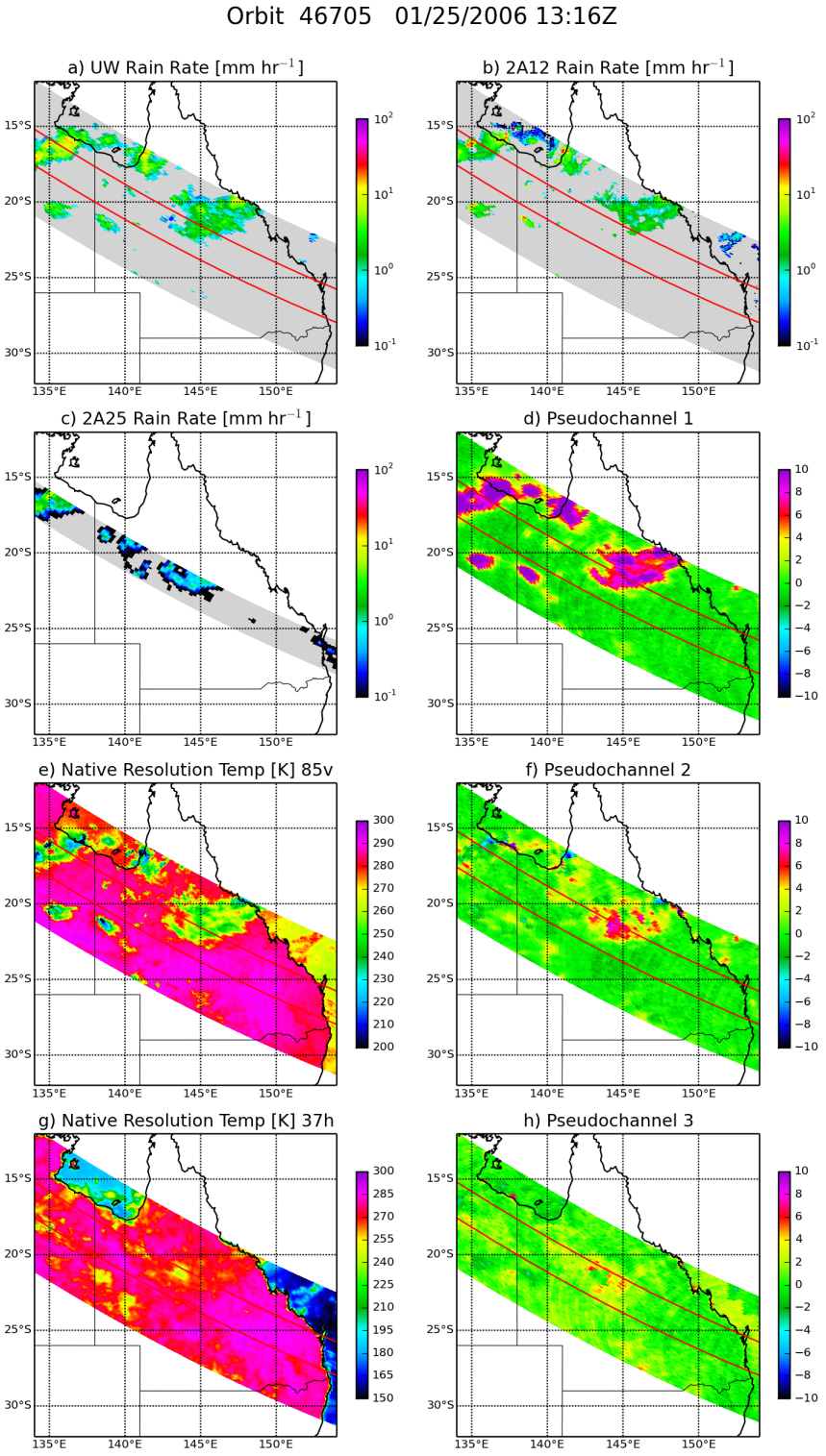

FIGURE 4.5: Swaths for Shallow MCS over north east Australia. TRMM orbit 46705.

rate match-ups when the precipitation event does not include enough variation from background. The pseudochannels are able to show clear variations in the background, even in cases of shallower convection, resulting from the PCA technique described in an earlier section. Based on the 85V channel, the north west rain activity is much more convective due to much cooler brightness temperatures, which is why both algorithms are performing better for that system.

4.1.6 Snow Over Land

The next precipitation event chosen to observe in this study is a snow over land case in the eastern part of China shown in Fig. 4.6. Because snow on the ground has similar radiative properties to ice particles aloft, many of these cases make retrievals difficult. The snow over land cases were chosen when the National Centers for Environmental Prediction (NCEP) reanalysis near-surface temperatures were colder than 268 K (Liu, personal communication). The results of this case are striking, as evidenced by 2A12 drastically missing the main precipitation event shown in the PR. 2A12 is still able to retrieve some precipitation signatures on the very east side of the swath. The UW algorithm is able to successfully calculate nearly all of the precipitation observed in the PR, with the exception of some light, very scattered precipitation to the west.

Temperatures in the 85V channel clearly contain relatively cold values compared to the background, yet only UW was able to successfully interpret the precipitation occurring. On the very west side of the swath there is a noticeably large ground

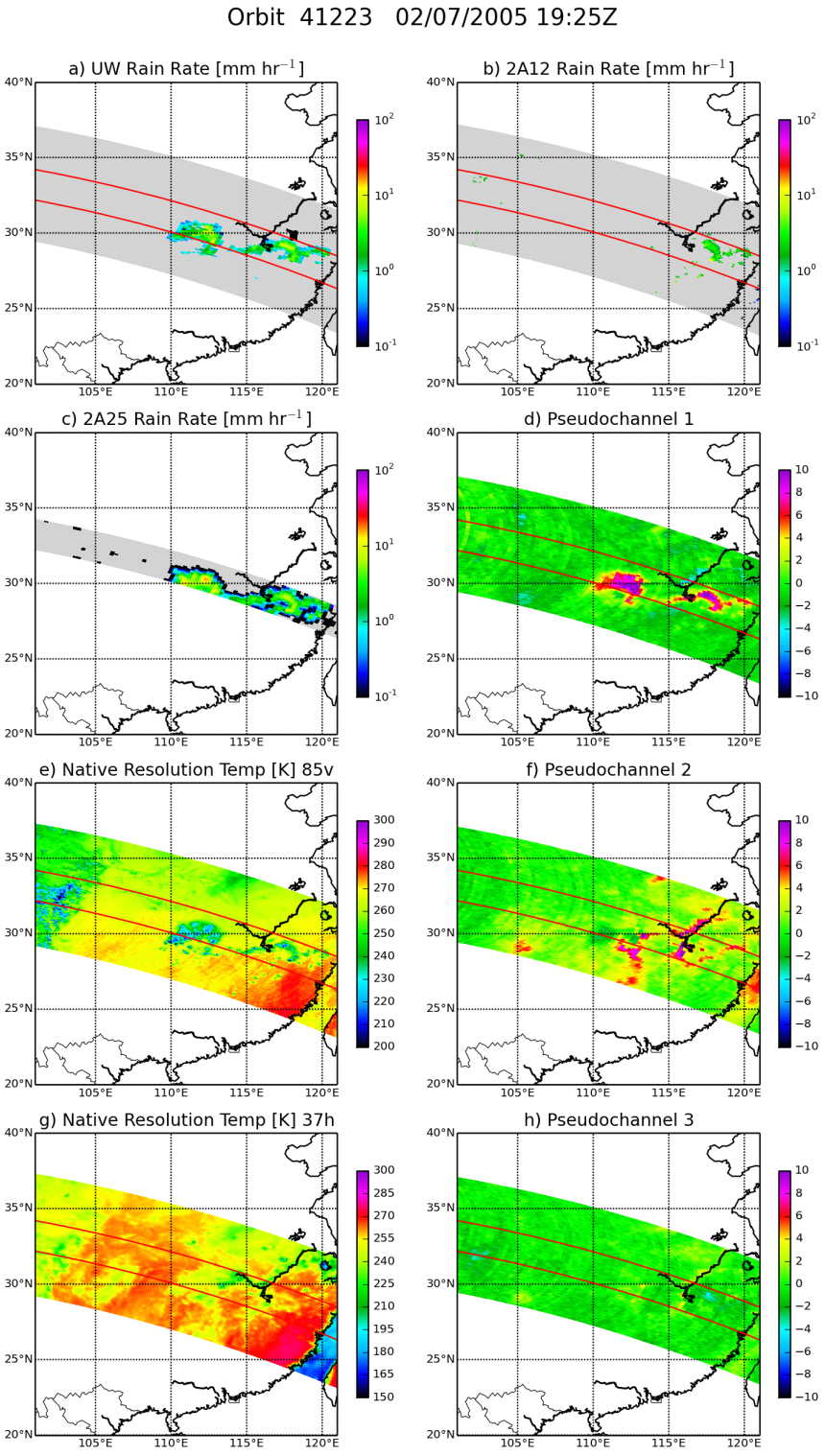

FIGURE 4.6: Swaths for a snow over land event over east China. TRMM orbit 41223.

temperature gradient and the region contains brightness temperatures cooler than the main event. This large gradient and cool brightness temperatures imply snow on the ground that the pseudochannels were able to successfully filter out as background geophysical noise, whereas 2A12's conservative nature most likely treated all cool temperatures as snow and filtered everything out including the actual precipitation. This is an exceptional example of how UW is able to interpret snow on the ground to snow falling.

4.1.7 Warm Rain Over Land

Another complex precipitation event described as warm rain over the eastern region of the Mediterranean is shown in Fig. 4.7. Lack of convection over moderate surface temperatures can make precipitation difficult to distinguish. Similar to the previous case, the initial results are striking. The 2A12 displays almost no rain occurring over land, whereas the PR shows significant rain occurring. Only a few pixels of precipitation are evident in the 2A12 swath associated with the highest rain rate in the PR. There is also distinct evidence of coastal artifacting occurring along the perimeter of the Mediterranean Sea. The UW algorithm, while also picking up fewer pixels of rain, displays much more of the relevant precipitation in the scene compared to the PR. Both algorithms neglect the light rain over the eastern border of Iraq, but UW is able to match up with the PR rain retrievals over the western region of Iran.

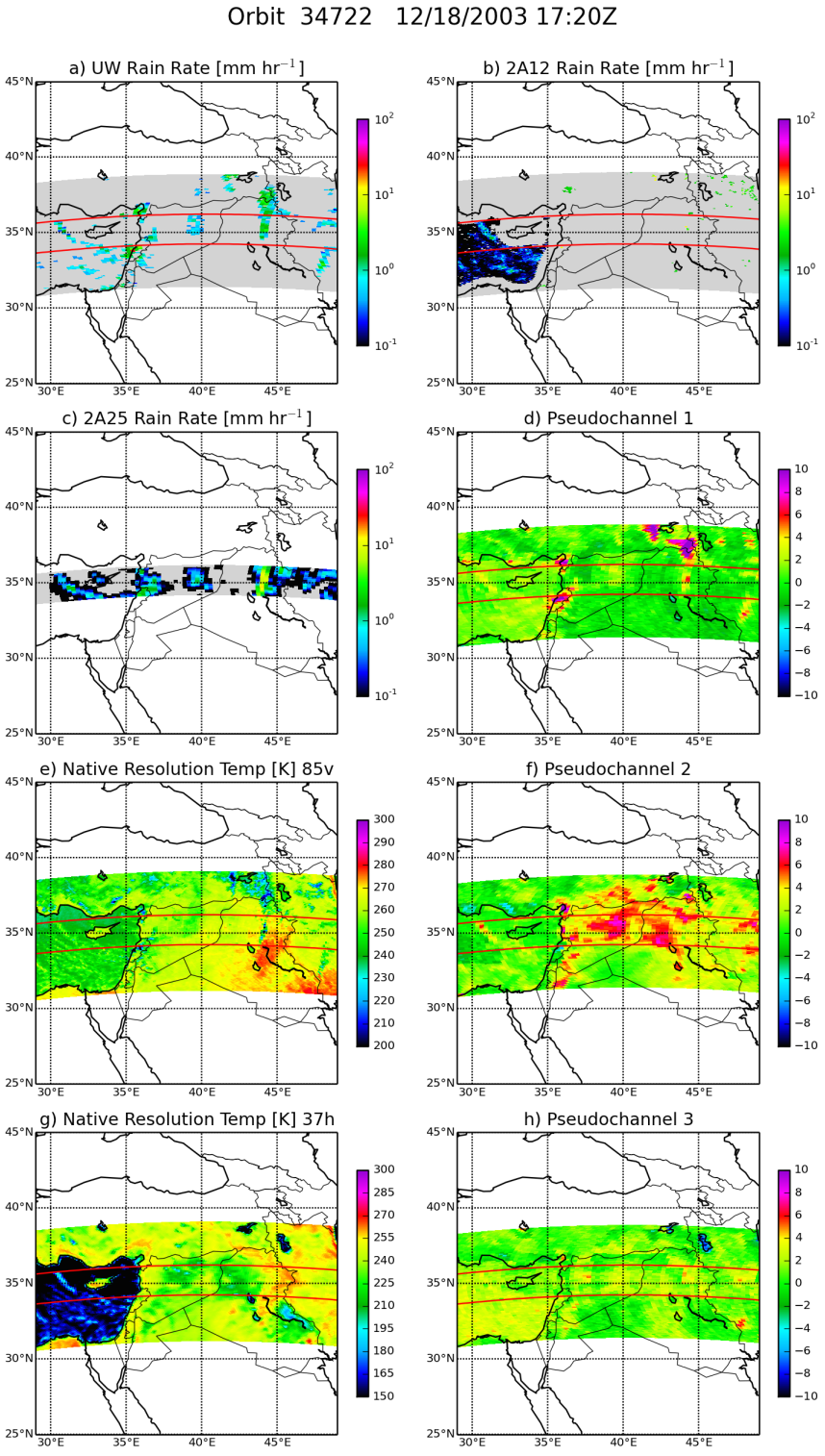

FIGURE 4.7: Swaths for a warm rain over land event over the east Mediterranean region. TRMM orbit 34722.

On the east coast of the Mediterranean, UW successfully calculates precipitation despite the temperature gradient between land and sea, which in this case is not as extreme. 85V temperatures show almost no convection occurring in this region, with the coldest measurements over Iraq. It is in this region that 2A12 finds a few pixels of rain over land, but is unsuccessful otherwise. In addition to the coastal artifacting, 2A12 displays continuous light rain over the majority of the Mediterranean Sea that is not evidenced by the PR. The 37H channel observes some warmer temperatures relative to the background that are associated with the higher rain rates over the sea in both 2A12 and UW, however UW does not misinterpret the rest of the region over the sea as raining. Warm rain over land is always difficult to measure, however for this particular case, the UW pseudochannels are able to successfully extract slight variations in background noise to provide a better representation of rainfall than the 2A12.

4.1.8 Rain Over Mountains

The next case discussed in this section involves a rainfall event over the Himalayan mountains just north of Nepal and shown in Fig. 4.8. Once again, the results are striking in the sense that 2A12 visibly neglects a significant amount of rain displayed in the PR swath. The main precipitation event in the center of the swath does not contain very intense rain rates, however a majority of the event is still depicted by the UW algorithm. The rainfall directly west of the main event is only slightly picked

up by UW near the most intense rain, but does not occur at all in 2A12. Another interesting aspect of this case is the rainfall shown in the PR at the most western edge of the swath. Neither UW or 2A12 signify any sort of rainfall existence in that location, and even the 85V shows no large disparity in brightness temperatures for the location. This might imply that even the radar is misinterpreting some information. This theory is suggested because cloud cover is not significantly apparent in the VIRS image (Fig 4.1g) either.

Taking another look at the 85V, there is a clear correspondence between the cooler brightness temperatures and the main precipitation event. The psuedochannels also show the most variance in the location of the main event, and the small variance to the west of the main event is also evident in the final UW calculation and corresponds to small temperature depressions in the 85V. In the southern portion of the swath there is a noticeably large temperature gradient on the edge of the mountains that both algorithms are both successfully able to filter out.

4.1.9 Rain Over Sahara Desert

One final case is visually observed. This last rainfall event takes place over the Sahara Desert and is shown in Fig. 4.9. The scattering properties of sand can influence the retrievals to wrongly predict precipitation. Perhaps the most striking event, this subtle rainfall band shown in the PR is completely neglected by 2A12. There are no visible pixels in the 2A12 swath at all, whereas UW is able to detect the narrow

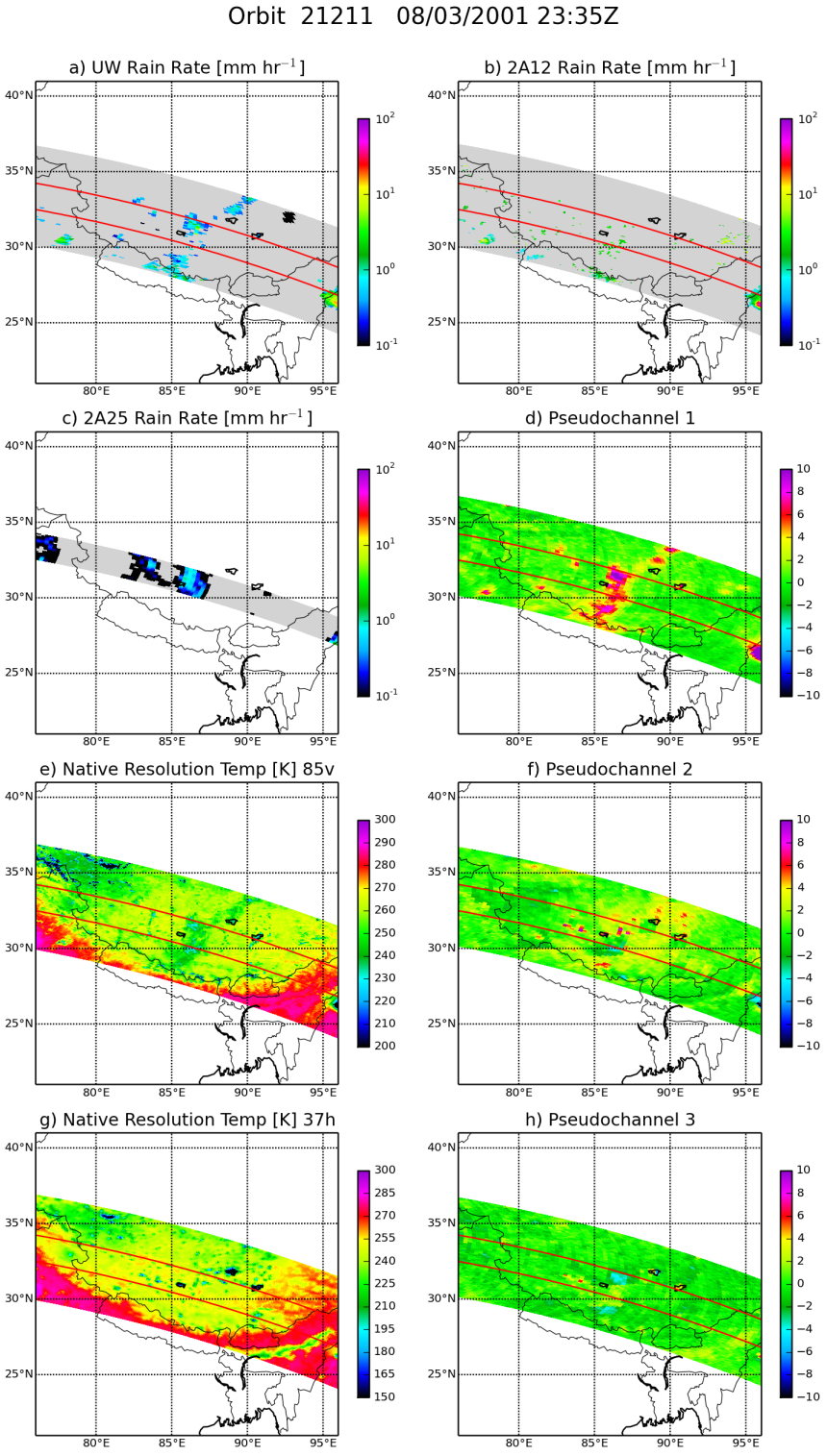

FIGURE 4.8: Swaths for a rain event over the Himalayan Mountains in southern China. TRMM orbit 21211.

band of rain. While the precipitation is visually observable in the UW swath, most of the rainfall is overestimated. The PR rain displays maximum rain rates below 1.0 millimeters per hour, and UW rain rates are on the order of a few millimeters per hour. The rain intensity difference is very apparent, yet the fact that UW is able to detect rain and 2A12 is not is very significant. Rain does not occur in deserts very often, and the ability for an algorithm to measure the small amounts of rain that does occur is important.

The 85V channel measures cooler brightness temperatures relative to the background, but there is little evidence that anything in the event is highly convective. Pseudochannel 1 shows most of the variance against the background geophysical noise, which corresponds to the UW algorithm database being densely populated enough to produce a more accurate rainfall measurement over the desert. Many of the other desert cases show similar results to this case. The rest of this section will take a look at the overall statistics for the combined cases for each category in an attempt to show the calculated differences between the two algorithms.

4.2 Statistics Results

In the following section, statistics for the above cases combined with all cases in that category will be discussed using the statistical concepts and comparisons described in Chapter 3.

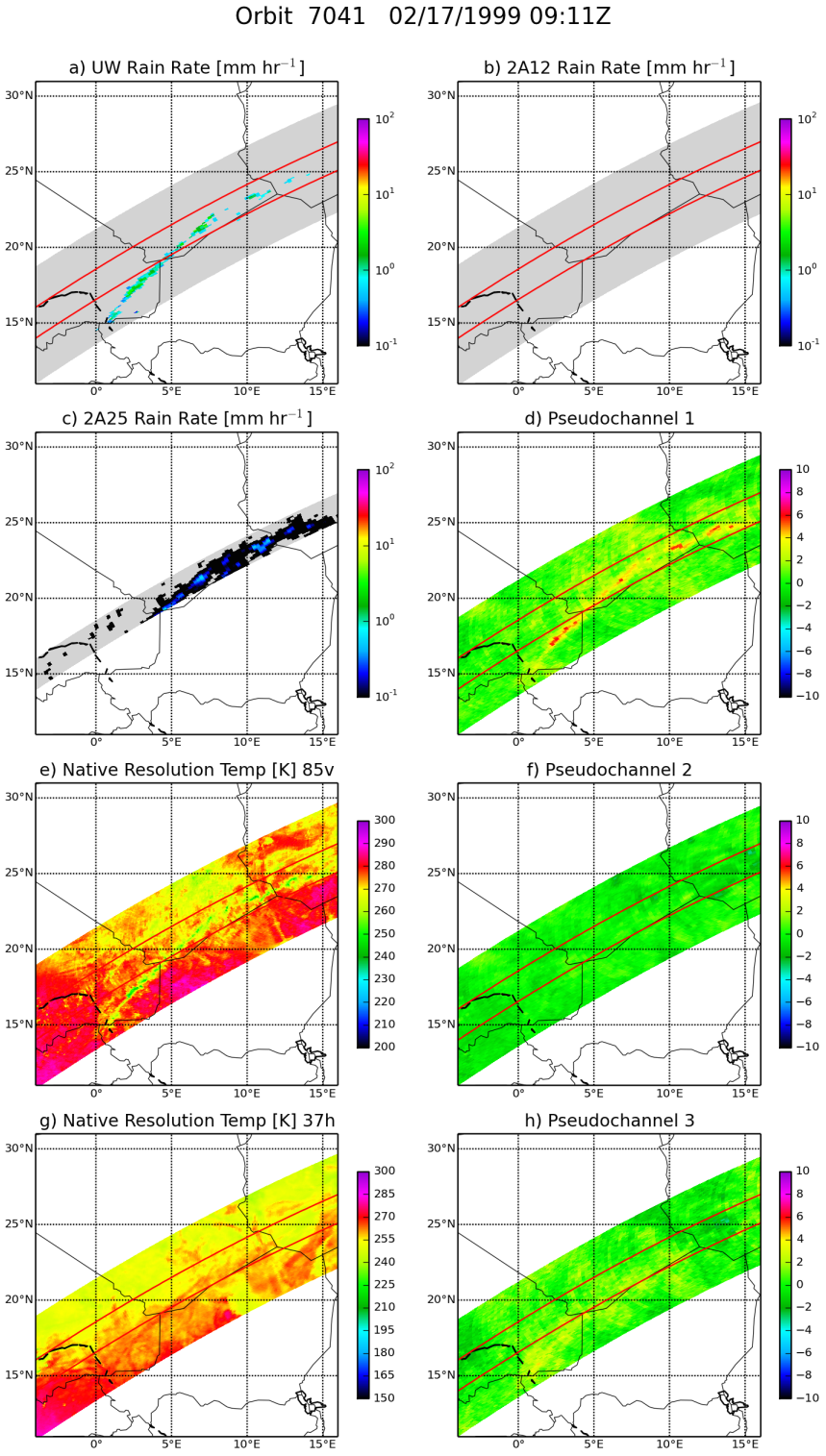

FIGURE 4.9: Swaths for a rain event over the Sahara Desert near the border of Algeria and Niger. TRMM orbit 7041.

4.2.1 Deep MCS China

The scatter plots shown in Fig. 4.10 displays the correlation between the UW rain rates and the PR measured rain rates (4.10a), as well as the 2A12 rain rates compared with the PR (4.10b). For added convenience, the scatter plots also display information about the number of pixels in the data (N), RMS, mean ratio, correlation coefficient (r), and HSS for 1.0 and 0.1 millimeter per hour thresholds. Log plots were chosen in order to conveniently display the smallest and largest rain rates together. From an initial observation of Fig. 4.10, UW looks to be more populated overall and is statistically performing better with a 55% decrease in RMS value, and a stronger correlation. Looking at the HSS, UW has better detection capabilities at both thresholds. An interesting note is that the accuracy of the HSS forecast for UW only decreases by 0.055 when detecting much lighter rain rates, whereas for 2A12, the difference is nearly 0.150 when detecting lighter rain rates. This implies that for Deep MCS events over China, UW is able to detect heavier and lighter rain rates with nearly the same accuracy, and 2A12 is much better at detecting higher rain intensities rather than low intensities.

4.2.2 Deep MCS Australia

Following the same trend as above, the scatter plots for the combined deep MCS Australia cases are shown in Fig. 4.11. Statistical analysis shows that the RMS

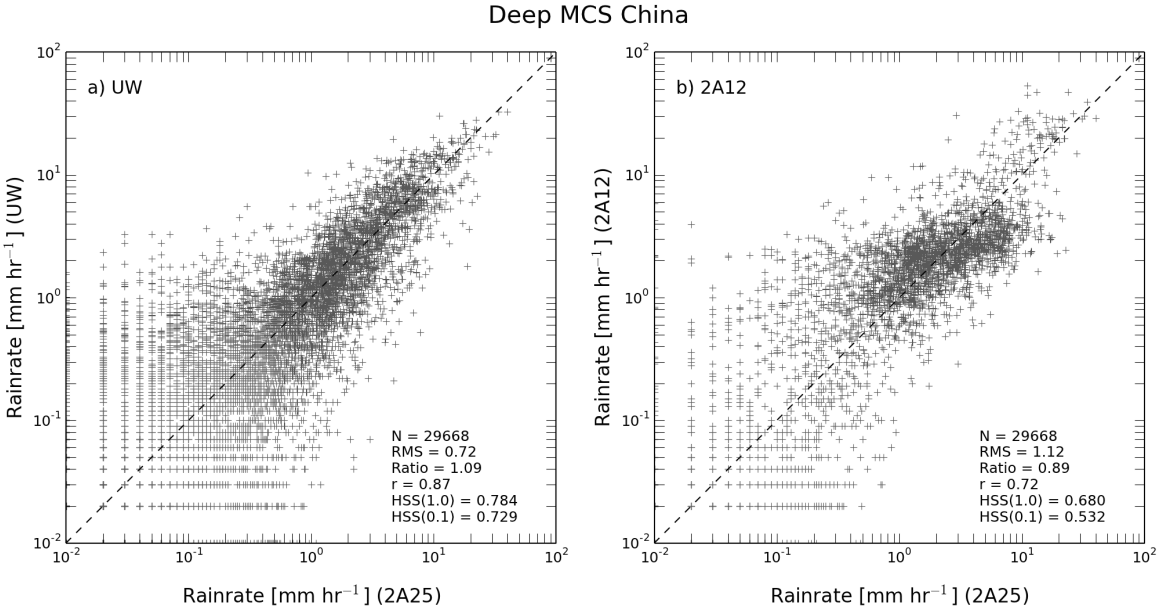

FIGURE 4.10: Scatter plots for data associated with deep MCS over China. Plots include separate comparisons of the UW algorithm (a) and GPROF algorithm (b) correlations with the PR. Also included are relevant statistics including number of pixels in the data (N), RMS, mean ratio, correlation coefficient (r), and HSS for 1.0 and 0.1 millimeter per hour thresholds.

for UW is about 77% better than 2A12. The correlations are closer for this case, yet the UW is still stronger than 2A12. Looking at the HSS, results are similar for both algorithms at the higher 1.0 millimeter per hour threshold with UW claiming a slightly stronger score, however this is very similar to the previous cases over China in that the 0.1 millimeter per hour threshold performs slightly worse than the higher value for UW, and much worse relative to the 2A12 higher value. So far in most deep convective cases, this has been common. Another interesting result shown in Fig 4.11 is that there are many 2A12 pixels that are associated with much higher rain rates than UW. This was evident in Fig. 4.3 where the 2A12 rain rates were shown to be much higher than what was depicted by the PR.

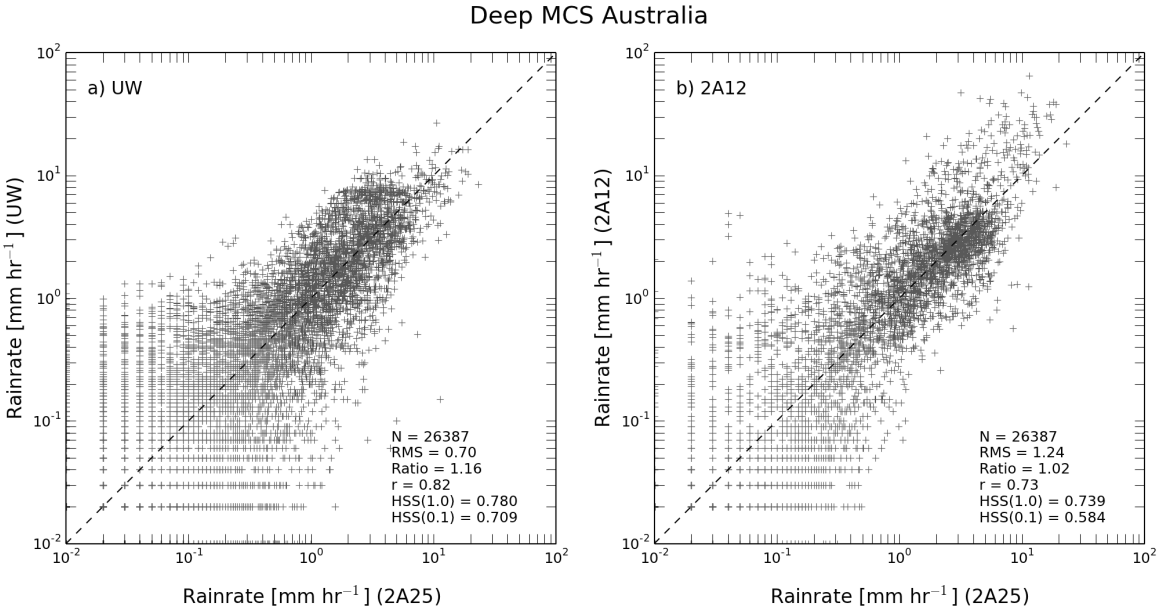

FIGURE 4.11: Scatter plots for data associated with deep MCS over Australia. Plots include separate comparisons of the UW algorithm (a) and GPROF algorithm (b) correlations with the PR. Also included are relevant statistics including number of pixels in the data (N), RMS, mean ratio, correlation coefficient (r), and HSS for 1.0 and 0.1 millimeter per hour thresholds.

4.2.3 Shallow MCS Central Africa

Moving on, the scatter plots for the combined shallow MCS over Central Africa cases are shown in Fig. 4.12. Once again, we see that the RMS value for the UW is about 42% lower than 2A12. The correlation coefficient is still stronger for UW as well. The HSS are more interesting for these cases in that UW maintains a high value for the larger threshold, but gets slightly weaker than before at the low threshold. Even more surprising is that for 2A12, while the HSS at both thresholds underperforms compared to UW, the lower threshold has a slightly higher score than the more intense rain rate score. The difference is not large, but unexpected nonetheless since smaller rain rates

are usually much more difficult to accurately calculate. Similar to the previous cases, the 2A12 rain rates are much higher than what the PR is measuring. This is evident since many pixels in Fig. 4.12b are above the correlation line at lower PR rain rates.

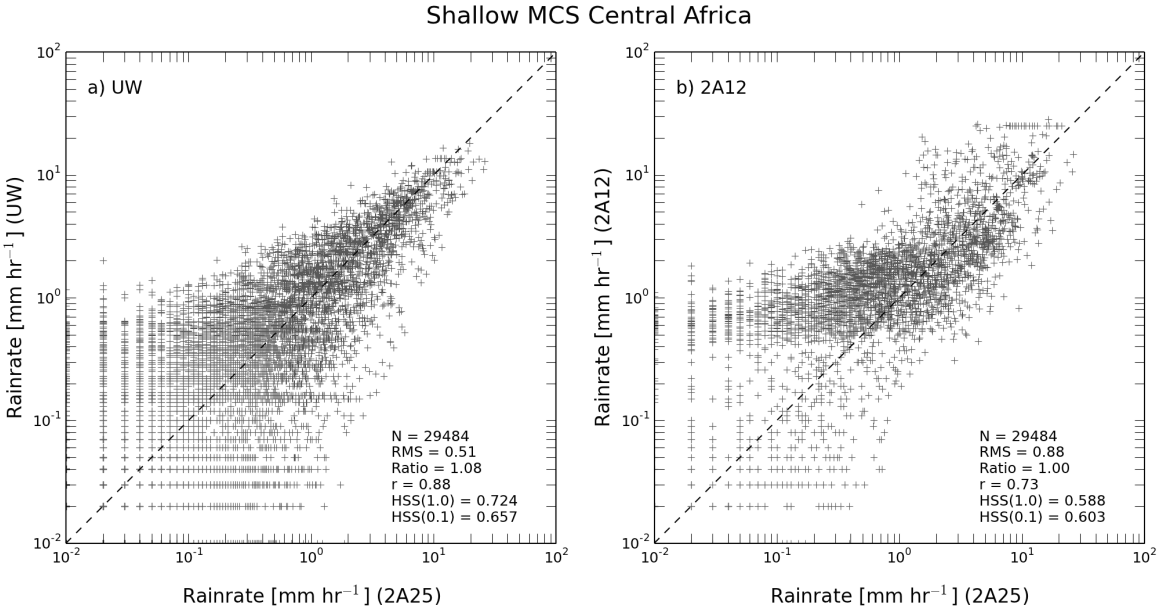

FIGURE 4.12: Scatter plots for data associated with shallow MCS over Central Africa. Plots include separate comparisons of the UW algorithm (a) and GPROF algorithm (b) correlations with the PR. Also included are relevant statistics including number of pixels in the data (N), RMS, mean ratio, correlation coefficient (r), and HSS for 1.0 and 0.1 millimeter per hour thresholds.

4.2.4 Shallow MCS Australia

Next, the scatter plots displaying statistical results for the combined shallow MCS cases over Australia are shown in Fig. 4.13. These cases are a particularly good example of the 2A12 performing comparably to UW. The RMS value is actually better for 2A12 in this case by a small margin, and the correlations are nearly the

same. The ratio suffers slightly for 2A12, but the main difference between the two algorithms for these cases are shown in the HSS. Like the RMS and correlation, the 1.0 millimeter per hour threshold values for both algorithms are nearly identical. The intense difference remains in 2A12's ability to detect rain rates near the lower threshold, which is significantly worse than UW, 0.701 compared to 0.476. Similar to the case described before this, but for the UW this time, is that the lower threshold score is higher than the larger threshold. It is surprising when this occurs, however, it is most likely due to the overall smaller rain rates that are associated with shallow MCS.

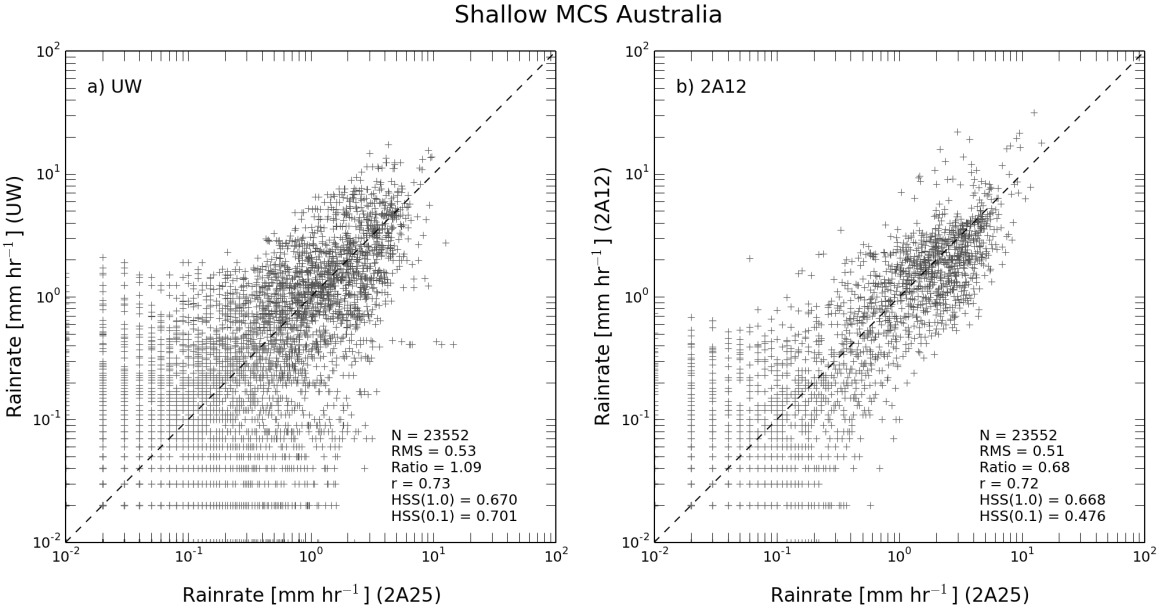

FIGURE 4.13: Scatter plots for data associated with shallow MCS over Australia. Plots include separate comparisons of the UW algorithm (a) and GPROF algorithm (b) correlations with the PR. Also included are relevant statistics including number of pixels in the data (N), RMS, mean ratio, correlation coefficient (r), and HSS for 1.0 and 0.1 millimeter per hour thresholds.

4.2.5 Snow Over Land

For the snow over land cases, the combined data and statistics are shown by the scatter plots in Fig. 4.14. Immediately noticeable in this case is the lack of active pixel density in the 2A12 compared to UW. This information explains that 2A12 misses a significant amount of precipitation when snow is likely present. The actual statistics show a lower RMS value for UW, as well as a significantly better correlation coefficient. Even more striking for the snow over land cases is the results of the HSS. The UW scores for both thresholds are very comparable, but overall they are slightly worse than for the convective cases. 2A12 HSS values are fairly dismal compared to UW as we see the lowest values so far of 0.350 for the large threshold and 0.240 for the low threshold. These scores are nearly reaching random characteristics of whether or not 2A12 can correctly forecast snow events compared to the PR.

4.2.6 Warm Rain Over Land

Next, the warm rain over land combined cases and statistics are shown by the scatter plots in Fig. 4.15. Visually there does not seem to be too much difference between the two algorithms interpretation of warm rain over land, but the statistics tell a different story. Similar to most of the cases above, RMS is much lower for UW, and once again, the correlation is much stronger. The HSS shows another significant difference between the two algorithms. UW maintains fairly consistent values near 0.600 for

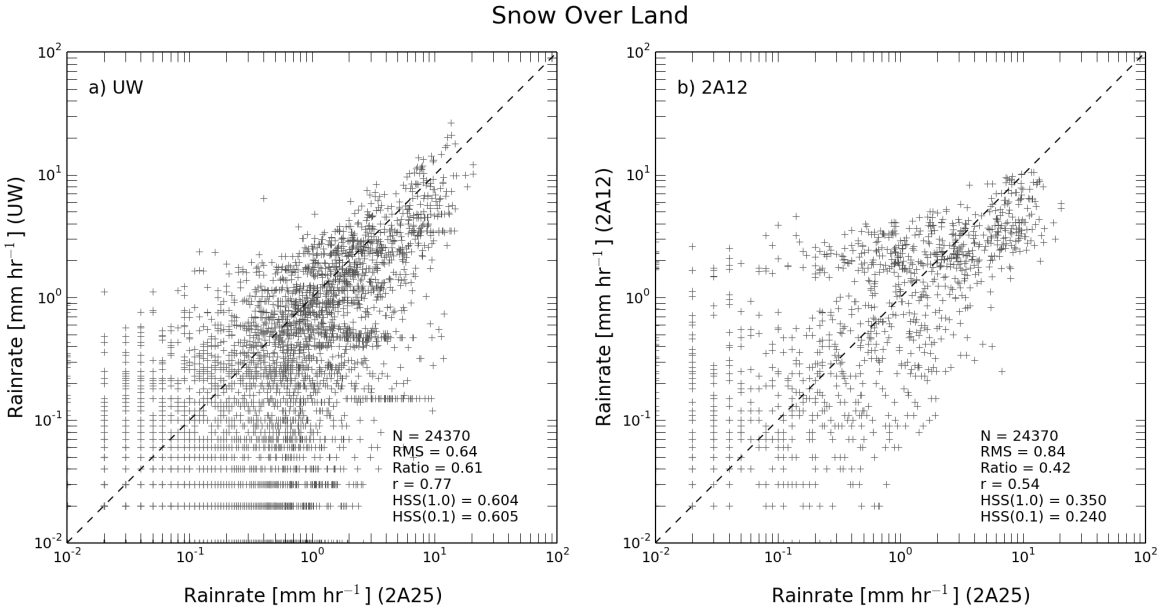

FIGURE 4.14: Scatter plots for data associated with snow over land. Plots include separate comparisons of the UW algorithm (a) and GPROF algorithm (b) correlations with the PR. Also included are relevant statistics including number of pixels in the data (N), RMS, mean ratio, correlation coefficient (r), and HSS for 1.0 and 0.1 millimeter per hour thresholds.

both thresholds of rain rate, however we see again that the low rain rate has a slightly better score. As mentioned before this is probably because warm rain systems lack large amounts of convection associated with more intense precipitation, so the system overall contains more small rain rates to measure or calculate. The HSS for 2A12 are lackluster again, but better than the snow over land cases, with the higher threshold producing a score of 0.433, and the low threshold producing a score of 0.385.

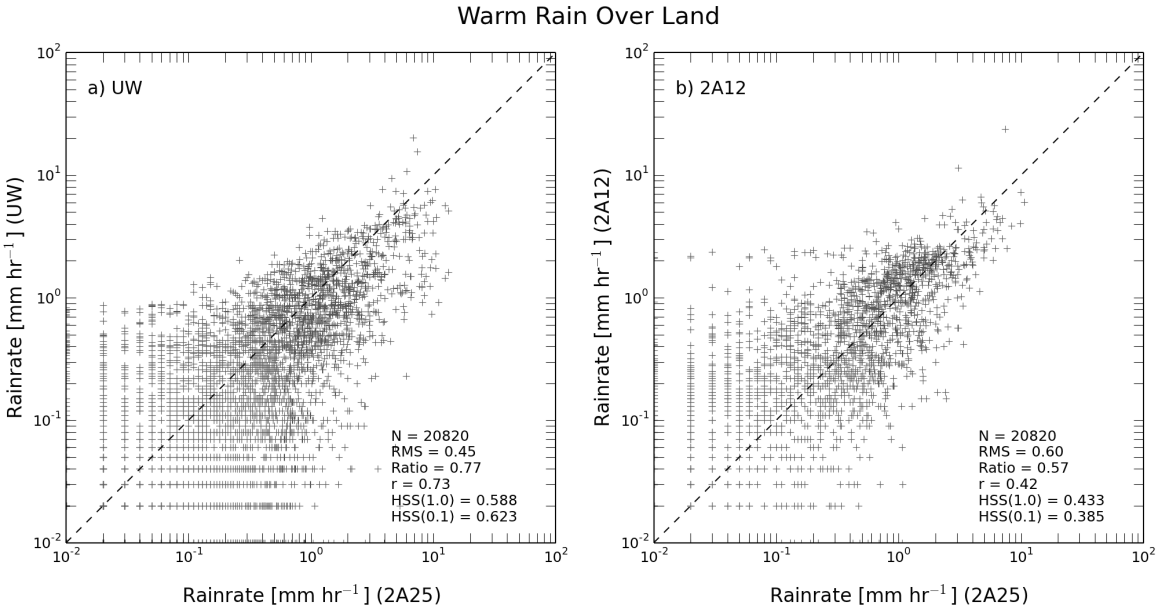

FIGURE 4.15: Scatter plots for data associated with warm rain over land. Plots include separate comparisons of the UW algorithm (a) and GPROF algorithm (b) correlations with the PR. Also included are relevant statistics including number of pixels in the data (N), RMS, mean ratio, correlation coefficient (r), and HSS for 1.0 and 0.1 millimeter per hour thresholds.

4.2.7 Rain Over Mountains

The combined statistics and scatter plots for the cases of rain occurring over mountains is shown in Fig. 4.16. An immediate visual difference within the plots is observed, showing that 2A12 tends to overestimate a majority of the rain rates below 1.0 millimeters per hour measured by the PR. Besides that, 2A12 is much improved in detecting rain over the mountains as compared to snow, and warm rain described above. Still, UW maintains a lower RMS value, and the correlation coefficient is still better. Population density of pixels also seems increased for UW overall. The HSS are improved for UW compared to snow and warm rain as well, and the values of

0.667 and 0.654 respectively for each thresholds are very comparable. 2A12 HSS at the high threshold is much better for these cases, however the low threshold scores are still less than ideal, and certainly well below the UW score.

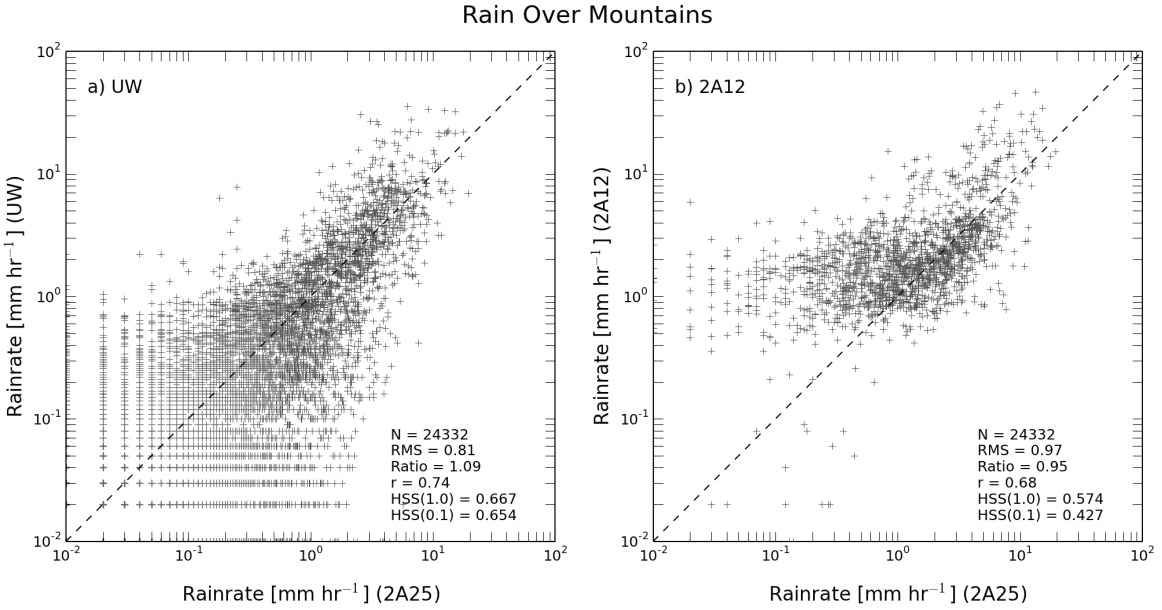

FIGURE 4.16: Scatter plots for data associated with rain over mountains. Plots include separate comparisons of the UW algorithm (a) and GPROF algorithm (b) correlations with the PR. Also included are relevant statistics including number of pixels in the data (N), RMS, mean ratio, correlation coefficient (r), and HSS for 1.0 and 0.1 millimeter per hour thresholds.

4.2.8 Rain Over Sahara Desert

Finally, the combined data and statistics for rain over the Sahara Desert are displayed by the scatter plots in Fig. 4.16. Probably the most striking visual results thus far, the 2A12 contains significantly fewer active pixels compared to the UW. The pixels that are evident in the 2A12 comparison are nearly all over the correlation line, meaning

that when 2A12 does detect some rain, it is nearly always overestimated. The statistics are also quite drastic. The RMS for UW is about 73% better, and the correlation is significantly stronger for UW as well. HSS hover just below 0.600 for both thresholds in the UW case, and again the lower threshold is slightly stronger due to desert rain systems not usually containing intense rain rates. The HSS for the high threshold in the 2A12 case comes in at just under 0.400, which is poor but not nearly as shocking as the low threshold score of 0.129. That low of a score is nearly the point of random chance whether or not 2A12 will calculate a rain rate for a given pixel.

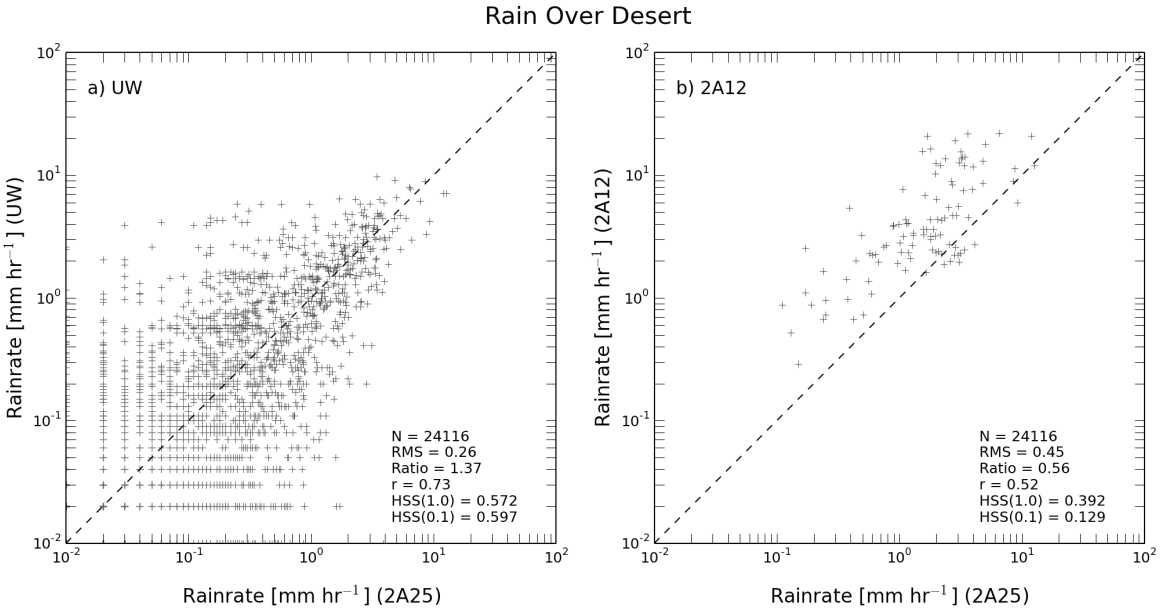

FIGURE 4.17: Scatter plots for data associated with rain over the Sahara Desert. Plots include separate comparisons of the UW algorithm (a) and GPROF algorithm (b) correlations with the PR. Also included are relevant statistics including number of pixels in the data (N), RMS, mean ratio, correlation coefficient (r), and HSS for 1.0 and 0.1 millimeter per hour thresholds.

TABLE 4.1: Summary of rainfall statistics for each category location associated with deep MCS.

	Ratio		RMS error		Correlation		HSS(1.0)		HSS(0.1)	
Deep MCS	UW	2A12	UW	2A12	UW	2A12	UW	2A12	UW	2A12
Central Africa	1.11	1.08	0.84	1.57	0.84	0.70	0.825	0.753	0.717	0.680
Amazon	0.90	0.87	0.72	1.22	0.85	0.71	0.736	0.672	0.661	0.462
SE US	0.94	0.71	0.71	1.03	0.86	0.72	0.800	0.720	0.769	0.462
SW US	0.92	0.81	0.79	1.32	0.86	0.68	0.815	0.704	0.779	0.586
Argentina	0.99	1.02	0.83	1.36	0.87	0.76	0.823	0.754	0.787	0.702
Indian	0.88	0.64	0.94	1.26	0.80	0.63	0.707	0.636	0.633	0.459
China	1.09	0.89	0.72	1.12	0.87	0.72	0.784	0.680	0.729	0.532
Maritime Cont.	0.90	0.84	0.69	1.19	0.84	0.69	0.747	0.686	0.720	0.564
Australia	1.16	1.02	0.70	1.24	0.82	0.73	0.780	0.739	0.709	0.584

4.3 Summary Tables

In an effort contain a repetitive and lengthy discussion for each category of cases, the above statistics as well as the statistics for each other category of cases is summarized in the proceeding tables. The number of cases associated with each location subtype is ten unless otherwise noted in the tables (N=X). Table 4.1 contains the desired information for each of the deep MCS location categories. A side-by-side comparison reveals that RMS for UW is significantly lower for all cases associated with deep MCS. Every correlation coefficient for UW is contained within the range of 0.80-0.87, whereas 2A12 values are in the range 0.63-0.76. HSS comparisons reveals that UW scores are consistently better than 2A12.

Similarly, the summary of statistics for each location in the shallow MCS category is displayed in Table 4.2. An overview of these statistics shows more scattered results that require a location specific analysis. The RMS values for UW are lower for every

TABLE 4.2: Summary of rainfall statistics for each category location associated with shallow MCS.

	Ratio		RMS error		Correlation		HSS(1.0)		HSS(0.1)	
Shallow MCS	UW	2A12	UW	2A12	UW	2A12	UW	2A12	UW	2A12
Central Africa	1.08	1.00	0.51	0.88	0.88	0.73	0.724	0.588	0.657	0.603
Amazon	0.91	0.69	0.67	0.81	0.78	0.69	0.677	0.575	0.572	0.419
SE US	0.79	0.73	0.41	0.59	0.88	0.75	0.765	0.701	0.725	0.569
SW US	0.75	0.47	0.53	0.70	0.82	0.64	0.725	0.571	0.713	0.414
Argentina	1.06	0.99	0.26	0.34	0.90	0.79	0.710	0.655	0.692	0.627
Indian	0.93	0.94	0.76	1.37	0.86	0.75	0.671	0.592	0.634	0.461
China	1.09	1.39	0.17	0.40	0.72	0.38	0.415	0.262	0.618	0.308
Maritime Cont.	1.00	0.90	0.60	0.86	0.92	0.84	0.748	0.719	0.670	0.659
Australia	1.09	0.68	0.53	0.51	0.73	0.72	0.670	0.668	0.701	0.476

location except over Australia where 2A12 has a slightly lower value. RMS values for UW range from 0.17-0.76, which is much larger than deep MCS, and 2A12 ranges from 0.34-1.37, also a much more drastic range. Correlation for UW is stronger in every location, as well as HSS for each threshold. Both algorithms seem to perform poorly for shallow MCS over China, especially for the 1.0 millimeter per hour threshold.

The statistical comparisons for deep ICS location categories are in Table 4.3. None of the deep ICS cases were shown in the above analysis because many of the swaths were difficult to observe visually as there were many small isolated rain systems populating a majority of the swath. Instead, it was decided that it would be much easier to compare the actual statistics instead of looking at the swaths side-by-side. Overall the values are somewhat striking. RMS statistics for 2A12 are much higher than UW, in many cases nearly three times the UW value. Similar to all previous categories and locations, the UW correlations are stronger than all 2A12 values. The same thing can be said for the HSS for both thresholds, and it is interesting to note the relatively poor

TABLE 4.3: Summary of rainfall statistics for each category location associated with isolated convective systems.

	Ratio		RMS error		Correlation		HSS(1.0)		HSS(0.1)	
Deep ICS	UW	2A12	UW	2A12	UW	2A12	UW	2A12	UW	2A12
Central Africa	1.69	2.35	0.78	2.30	0.84	0.73	0.693	0.630	0.657	0.364
Amazon	0.94	1.28	0.59	1.81	0.81	0.58	0.663	0.589	0.563	0.302
SE US	1.23	1.79	0.60	1.69	0.81	0.69	0.773	0.635	0.612	0.388
SW US	0.68	1.19	0.44	1.18	0.77	0.66	0.625	0.551	0.574	0.296
Argentina	0.95	1.27	0.57	1.41	0.87	0.72	0.760	0.682	0.637	0.535
Indian	0.84	1.24	0.64	1.76	0.77	0.62	0.675	0.593	0.603	0.384
China	0.94	1.15	0.50	1.30	0.83	0.63	0.699	0.566	0.548	0.314
Maritime Cont.	1.03	1.24	0.52	1.53	0.80	0.61	0.673	0.587	0.625	0.405
Australia	1.12	1.71	0.49	1.44	0.81	0.74	0.696	0.613	0.620	0.411

TABLE 4.4: Summary of rainfall statistics for each extra category location.

	Ratio		RMS error		Correlation		HSS(1.0)		HSS(0.1)	
Other	UW	2A12	UW	2A12	UW	2A12	UW	2A12	UW	2A12
Snow Land (N=8)	0.61	0.42	0.64	0.84	0.77	0.54	0.604	0.350	0.605	0.240
Snow Ocean (N=9)	0.77	0.75	0.38	0.41	0.81	0.78	0.562	0.544	0.568	0.547
Warm Rain Land (N=8)	0.77	0.57	0.45	0.60	0.73	0.42	0.588	0.433	0.623	0.385
Mountain (N=8)	1.09	0.95	0.81	0.97	0.74	0.68	0.667	0.574	0.654	0.427
Sahara Desert (N=9)	1.37	0.56	0.26	0.45	0.73	0.52	0.572	0.392	0.597	0.129

values for 2A12 HSS at the 0.1 millimeter per hour threshold. UW has an average low threshold score of 0.604 where 2A12's mean score is 0.378.

Finally, the last few location category statistics are shown in Table 4.4. Many examples of these locations were shown in the visual analysis, however it is shown again that RMS values for UW are consistently lower than 2A12. Correlations are all very similar for UW and once again stronger than the 2A12 values. All of the UW skill scores are also better than 2A12, and is especially apparent in for Sahara Desert cases, which has already been discussed earlier in this section.

Chapter 5

Summary and Future Work

5.1 Summary and Conclusions

Two different algorithms have been used to calculate rain rates over a variety of surface classes and are compared against each other. The GPROF algorithm, which is based on the SSM/I algorithms from the late 1980s, is the current NASA standard product for calculating rain rates via the TRMM satellite microwave imager. GPROF uses a populated nine-dimensional database that contains rain rates associated with TMI brightness temperatures. The new UW algorithm, developed by Grant Petty at the University of Wisconsin-Madison, employs the use of a two-stage principle component analysis to create a more densely populated rain rate database corresponding

to measured brightness temperatures, and has previously been shown to better measure annual rainfall in the tropics. This research has narrowed in on over 300 case studies over specific locations to more closely analyze when and how much the UW algorithm has improved precipitation measurements over the tropics. The many cases observed included nine different locations associated with deep MCS, shallow MCS, and deep ICS. An additional five categories were included to observe snow, and rain over mountains and deserts.

The results of the experiment were shown by selecting a few of the cases that displayed dramatic visual differences between algorithms, and they were compared with the more reliable, higher resolution precipitation radar product, which is much better at detecting lighter rain rates. In addition to the PR, swaths from the TMI 85V and 37H channel were used as indicators for intense convective regions, and distinguishing rain water from cloud water respectively. The three pseudochannel products resulting from the UW's principal component analysis was also shown to imply the variance from the background that was extracted. An infrared image from VIRS data was also shown in order to reference the cloud distribution for each swath. Scatter plots of the selected swaths were able to show how each algorithm correlated to the PR, and in some cases was able to display intense differences in raining pixel density.

While many individual swaths were quite comparable between algorithms, there were some striking findings that can not be ignored. The first of which is that for all but one location category, the UW algorithm had consistently lower RMS values,

and for the one different case, the discrepancy in RMS was 0.02. Not only were the RMS values better for UW, every correlation coefficient for every category location was stronger, sometimes markedly better than 2A12. The HSS, being an excellent indicator of an algorithms ability to correctly identify a raining pixel above a given threshold was, in 100% of combined cases, better for UW. The most apparent case being for the combined statistics over the Sahara Desert where at the 0.1 millimeter per hour threshold, UW had a score of 0.587, and 2A12 mustered up an abysmal 0.129, implying a nearly random chance that 2A12 would correctly associate a raining pixel over the desert.

It is important to reiterate that over 300 individual cases were observed, and for many of the cases, the algorithms were very comparable visually, although a significant portion of 2A12 observations displayed coastal artifacting, where UW showed none. Statistically overall, it can be said with confidence that the UW algorithm method performs better than 2A12 V7 at least for these cases.

5.2 Future Work

While over 300 cases were observed in this experiment, comparisons between these algorithms, as well as with other products is never complete. With the conclusion of the TRMM era having passed, there is much work that must be done to apply and improve the UW product for the recently launched GPM instruments. Now that

the new satellite is able to span the latitudes of 60°S to 60°N, a variety of surface combinations are added, for example: significantly more snow on the ground will be observed, and mixes of snow, coniferous forests and tundra will also pose problems for algorithm interpretation. The GMI also contains 13 channels instead of nine on TMI, so the dimensional reduction procedure will have more channels to diminish and may require alternate coefficients when applying the two-stage PCA and successfully populating a fewer amount of channels.

This study was also limited to cases over 9 locations plus a few individual regions, and is by no means a complete analysis of all areas observed by TRMM. The multitude of locations helps to generalize our understanding of the functionality of the two algorithms. However there is the always an opportunity to include a greater representation of tropical regions. It is also important to reiterate that the PR is not a perfect instrument. Both algorithms were compared to a product that has its own limitations and errors, but is overall considered to be much more accurate. These algorithms could also be subjected to ground based validation in an attempt to provide more robust results.

Bibliography

Adler, R. F., C. Kidd, G. Petty, M. Morrissey, and H. M. Goodman, 2001: Intercomparison of Global Precipitation Products: The Third Precipitation Intercomparison Project (PIP-3). *Bull. Amer. Meteor. Soc.*, **82**, 1377–1396.

Adler, R. F., A. J. Negri, and I. M. Hakkarinen, 1991: Rain Estimation from Combining Geosynchronous IR and Low-Orbit Microwave Data. *Global Planet. Change*, **90**, 87–92.

Anagnostou, E. N., A. J. Negri, and R. F. Adler, 1999: A Satellite Infrared Technique for Diurnal Rainfall Variability Studies. *J. Geophys. Res.*, **104**, 31,477–31,488.

Barrett, E. and Coauthors, 1994: The First WetNet Precipitation Intercomparison Project: Interpretation of Results. *Remote Sens. Rev.*, **11**, 303–373.

Chiu, L. S., G. R. North, D. A. Short, and A. McConnell, 1990: Rain Estimation from Satellites: Effect of Finite Field of View. *J. Geophys. Res.*, **95**, 2177–2185.

Conner, M. D. and G. W. Petty, 1998: Validation and Intercomparison of SSM/I Rain-Rate Retrieval Methods over the Continental United States. *J. Appl. Meteor.*, **37**, 679–700.

Creutin, J. D., G. Delrieu, and T. Lebel, 1988: Rain Measurement by Rainguage-Radar Combination: A Geostatistical Appraoch. *J. Atmos. Oceanic Technol.*, **5**, 102–115.

Doswell, C., R. Davies-Jones, and D. Keller, 1990: On Summary Measures of Skill in the Rare Event Forecasting Based on Contingency Tables. *Wea. Forecasting*, **5**, 576–585.

Ebert, E., M. Manton, P. Arkin, R. Allam, G. Holpin, and A. Gruber, 1996: Results from the GPCP Algorithm Intercomparison Programme. *Bull. Amer. Meteor. Soc.*, **77**, 2875–2887.

Evans, K. F., J. Turk, T. Wong, and G. L. Stephens, 1995: A Bayesian Approach to Microwave Precipitation Profile Retrieval. *J. Appl. Meteor.*, **34**, 260–279.

Ferraro, R. and coauthors, 2013: An Evaluation of Microwave Land Surface Emissivities Over the Continental United States to Benefit GPM-Era Precipitation Algorithms. *IEEE Trans. Geosci. Remote Sens.*, **51**, 378–398.

Gloerson, P. and F. T. Barath, 1977: A Scanning Multichannel Microwave Radiometer for Nimbus-G and SeaSat-A. *IEEE J. Ocean. Eng.*, **2**, 172–178.

Gopalan, K., N. Wang, R. Ferraro, and C. Liu, 2010: Status of the TRMM 2A12 Land Precipitation Algorithm. *J. Atmos. Oceanic Technol.*, **27**, 1343–1354.

Grody, N. C., 1991: Classification of Snow Cover and Precipitation Using the Special Sensor Microwave Imager. *J. Geophys. Res.*, **96**, 7423–7435.

Heidke, P., 1926: Berechnung des erfolges und der güte der windstärke-vorhersagen in sturmwarnungsdienst. *Geogr. Ann.*, **8**, 301–349.

Huffman, G. J., et al., 1997: The Global Precipitation Climatology Project (GPCP) Combined Precipitation Dataset. *Bull. Amer. Meteor, Soc.*, **78**, 5–20.

Jeyaseelan, A. T., 2003: Droughts and Floods Assessment And Monitoring Using Remote Sensing and GIS. *Sat. Rem. Sens. GIS Appl. Agr. Meteor.*, 291–313.

Johnson, B. T., G. W. Petty, and G. Skofronick-Jackson, 2012: Microwave Properties of Ice-Phase Hydrometeors for Radar and Radiometers: Sensitivity to Model Assumptions. *J. Appl. Meteor. Climat.*, **51**, 2152–2171.

Kummerow, C., W. Barnes, T. Kozu, J. Shiue, and J. Simpson, 1998: The Tropical Rainfall Measuring Mission (TRMM) Sensor Package. *J. Atmos. Oceanic Technol.*, **15**, 809–817.

Kummerow, C. and coauthors, 2000: The Status of the Tropical Rainfall Measuring Mission (TRMM) after Two Years in Orbit. *J. Appl. Meteor.*, **39**, 1965–1982.

Kummerow, C. and coauthors, 2001: The Evolution of the Goddard Profiling Algorithm (GPROF) for Rainfall Estimation from Passive Microwave Sensors. *J. Appl. Meteor,*, **40**, 1801–1820.

Kummerow, C. and L. Giglio, 1994a: A Passive Microwave Technique for Estimating Rainfall and Vertical Structure Information from Space Part I: Algorithm Description. *J. Appl. Meteor.*, **33**, 19–34.

Kummerow, C., R. A. Mack, and I. M. Hakkarinen, 1989: A Self-Consistency Approach to Improve Microwave Rainfall Rate Estimation from Space. *J. Appl. Meteor.*, **28**, 869–884.

Kummerow, C. D., S. Ringerud, J. Crook, D. Randel, and W. Berg, 2011: An Observationally Generated A Priori Database for Microwave Rainfall Retrievals. *J. Atmos. Oceanic Technol.*, **28**, 113–130.

Liebe, H. J., G. A. Hufford, and M. G. Cotton, 1993: Propagation Modeling of Moist Air and Suspended Water/Ice Particles at Frequencies below 1000 GHz. *AGARD Conf. Proc.*, **542**, 3.1–3.10.

McCollum, J. R. and R. R. Ferraro, 2005: Microwave Rainfall Estimation over Coasts. *J. Atmos. Oceanic. Technol.*, **22**, 497–512.

Meehl, G. A. and coauthors, 2007: Contributions of Working Group I to the Fourth Assessment Report of the Intergovernmental Panel on Climate Change. *IPCC*, **4**.

Mugnai, A. and E. A. Smith, 1988: Radiative Transfer to Space through a Precipitating Cloud at Multiple Microwave Frequencies. Part I: Model Description. *J. Appl. Meteor.*, **27**, 1055–1073.

Pearson, K., 1895: Note on Regression and Inheritance in the Case of Two Parents. *The Royal Society*, **58**, 240–242.

Petty, G., 1994a: Physical Retrievals of Over-Ocean Rain Rate from Multichannel Microwave Imagery. Part I: Theoretical Characteristics of Normalized Polarization and Scattering Indices. *Meteor. Atmos. Phys*, **54**, 79–100.

Petty, G. W., 1995: The Status of Satellite-Based Rainfall Estimation over Land. *Remote Sens. Environ.*, **51**, 125–137.

Petty, G. W., 2013: Dimensionality Reduction in Bayesian Estimation Algorithms. *Atmos. Meas. Tech.*, **6**, 2267–2276.

Petty, G. W. and K. B. Katsaros, 1992: The Response of the SSM/I to the Marine Environment. Part I: An Analytic Model for the Atmospheric Component of Observed Brightness Temperatures. *J. Atmos. Oceanic Technol.*, **9**, 746–761.

Petty, G. W. and K. Li, 2013a: Improved Passive Microwave Retrievals of Rain Rate over Land and Ocean. Part I: Algorithm Description. *J. Atmos. Oceanic Technol.*, **30**, 2493–2508.

Petty, G. W. and K. Li, 2013b: Improved Passive Microwave Retrievals of Rain Rate over Land and Ocean. Part II: Validation and Intercomparison. *J. Atmos. Oceanic Technol.*, **30**, 2509–2526.

Schols, J., J. Weinman, G. Alexander, R. Stewart, L. Angus, and A. Lee, 1999: Microwave Properties of Frozen Precipitation Around a North Atlantic Cyclone. *J. Appl. Meteor.*, **38**, 29–43.

Simpson, J., R. F. Adler, and G. R. North, 1988: A Proposed Tropical Rainfall Measuring Mission (TRMM) Satellite. *Bull. Amer. Meteor. Soc.*, **69**, 278–295.

Simpson, J., C. Kummerow, W. K. Tao, and R. Adler, 1996: On the Tropical Rainfall Measuring Mission (TRMM). *Meteorol. Atmos. Phys.*, **60**, 19–36.

Smith, E. A. and coauthors, 1998: Results of WetNet PIP-2 project. *J. Atmos. Sci.*, **55**, 1483–1536.

Smith, E. A. and coauthors, 2007: International Global Precipitation Measurement (GPM) Program and Mission: An Overview. *EURAINSAT and the Future*, **28**, 611–653.

Smith, E. A., A. Mugnai, H. J. Cooper, G. J. Tripoli, and X. Xiang, 1992: Foundations for Statistical-Physical Precipitation Retrieval from Passive Microwave Satellite Measurements. Part I: Brightness-Temperature Properties of a Time-dependent Cloud Radiation Model. *J. Appl. Meteor.*, **31**, 506–531.

Spencer, R. W., 1986: A Satellite Passive 37-GHz Scattering-based Method for Measuring Oceanic Rain Rates. *J. Climate Appl. Meteor.*, **25**, 754–766.

Spencer, R. W., H. M. Goodman, and R. E. Hood, 1989: Precipitation Retrieval over Land and Ocean with the SSM/I: Identification and Characteristics of the Scattering Signal. *J. Atmos. Oceanic Technol.*, **6**, 254–273.

Spencer, R. W., B. B. Hinton, and W. S. Olson, 1983: Nimbus-7 37 GHz Radiances Correlated with Radar Rain Rates Over Land. *Nature*, **304**, 141–143.

Sudradjat, A., N. Y. Wang, K. Gopalan, and R. R. Ferraro, 2011: Prototyping a Generic, Unified Land Surface Classification and Screening Methodology for GPM-Era Microwave Land Precipitation Retrieval Algorithms. *J. Appl. Meteor. Climat.*, **50**, 1200–1211.

Tao, W. K. and coauthors, 2001: Retrieved Vertical Profiles of Latent Heat Release using TRMM Rainfall Products for February 1988. *J. Appl. Meteor.*, **40**, 957–982.

Todd, M. C., C. Kidd, D. Kniveton, and T. J. Bellerby, 2001: A Combined Satellite Infrared and Passive Microwave Technique for Estimation of Small-Scale Rainfall. *J. Atmos. Oceanic Technol.*, **18**, 742–755.

Trenberth, K. E., 1999: Conceptual Framework for changes of Extremes of the Hydrological Cycle with Climate Change. *Climatic Change*, **42**, 327–339.

Trenberth, K. E., J. T. Fasullo, and J. Kiehl, 2009: Earth's Global Energy Budget. *Bull. Amer. Meteor. Soc.*, **90**, 311–323.

Vivekanandan, J., J. Turk, G. L. Stephens, and V. N. Bringi, 1990: Microwave Radiative Transfer Studies Using Combined Multiparameter Radar and Radiometer Measurements during COHMEX. *J. Appl. Meteor.*, **29**, 561–585.

Wang, N. Y., C. Liu, R. Ferraro, D. Wolff, E. Zipser, and C. Kummerow, 2009: TRMM 2A12 Land Precipitation Product - Status and Future Plans. *J. Meteor. Soc. Jap.*, **87A**, 237–253.

Weinman, J. A. and P. J. Guetter, 1977: Determination of Rainfall Distribution from Microwave Radiation Measured by the Nimbus 6 ESMR. *J. Appl. Meteor.*, **16**, 437–442.

Wilheit, T. T., A. T. C. Chang, M. S. V. Rao, E. B. Rodgers, and J. S. Theon, 1977: A Satellite Rechnique for Quantitatively Mapping Rainfall Rates over the Oceans. *J. Appl. Meteor.*, **16**, 551–560.

Wilheit, T. T., J. S. Theon, W. E. Shenk, and L. J. Allison, 1976: Meteorological Interpretations of the Images from the Nimbus 5 Electrically Scanned Microwave Radiometer. *J. Appl. Meteor*, **15**, 166–172.

Xie, P. and P. A. Arkin, 1997: Global Precipitation: A 17-Year Monthly Analysis Based on Gauge Observations, Satellite Estimates, and Numerical Model Outputs. *Bull. Amer. Meteor. Soc.*, **78**, 2539–2558.